QUANTITATIVE PHASE IMAGING OF FIBER BRAGG GRATINGS

A Thesis
Presented to
The Academic Faculty

By

Grayson M. Noah

In Partial Fulfillment
Of the Requirements for the Degree
Master of Science in Electrical and Computer Engineering

Georgia Institute of Technology
May 2019

QUANTITATIVE PHASE IMAGING OF FIBER BRAGG GRATINGS

Approved by:

Dr. Thomas K. Gaylord, Advisor
School of Electrical and Computer Engineering
Georgia Institute of Technology

Dr. Lukas Graber
School of Electrical and Computer Engineering
Georgia Institute of Technology

Dr. Benjamin D. B. Klein
School of Electrical and Computer Engineering
Georgia Institute of Technology

Dr. Sorin Tibuleac
ADVA Optical Networking

Date Approved: April 23, 2019

ACKNOWLEDGEMENTS

This work is a testament to the people who have supported me over its development and throughout my life. Without these people, this work would not exist, and I would not be the person I am today.

Firstly, I thank Dr. Tom Gaylord, my thesis advisor, teacher, and friend, for his guidance through this process. His exemplification of excellence in academic pursuits, physical wellness, and human character is always an inspiration.

I would additionally like to thank each of the other members of my thesis committee: Dr. Ben Klein, Dr. Lukas Graber, and Dr. Sorin Tibuleac. Their insight, feedback, and questioning helped shape this thesis into the complete form it now takes. Each of them shares a passion and excitement for learning that makes them fabulous researchers and teachers, and I'm honored to have them as my committee members.

Yijun Bao, my fellow researcher in the Georgia Tech Optics Lab, has been instrumental in helping me learn and accomplish what was necessary for this research as my work progressed alongside and following his own. I owe him many thanks for setting the stage for my research and being eager to assist along the way.

I would like to thank Technica Optical Components and FemtoFiberTec GmbH for directly supporting my research by providing the FBG samples imaged in this research.

I thank my parents, Scott and Mimi, for instilling the values that guide me and providing more kinds of support than I can count through every stage of my life. I thank my sister, Kate, for being a model of selflessness and someone I can always count on.

I thank Tessa Valentien for being my partner in life and my best friend. She motivates me to strive for greater things and dream big. I am grateful beyond words for all she does and all she is.

GRAYSON M. NOAH

TABLE OF CONTENTS

LIST OF TABLES

LIST OF FIGURES

LIST OF SYMBOLS

$A(\vec{r})$	Imaginary part of scattering potential (spatial absorption function)
$A(\vec{\rho})$	Fourier transform of imaginary part of scattering potential
α	Absorption coefficient
B	Bandwidth
d	Grating length
Δh	Surface relief ridge height
Δn	Refractive index difference
$\Delta n_{\mathrm{B}}(\vec{r})$	Background variation in refractive index
$\Delta\varphi$	Phase difference
Δx	Pixel spacing in the x-direction
Δy	Pixel spacing in the y-direction/effective camera resolution
$\delta(\ \ )$	Dirac delta function
δy	Effective pixel spacing in the y-direction after upsampling
η	Diffraction efficiency (reflectivity of Bragg grating)
FF_x	Pixel fill factor in the x-direction
FF_y	Pixel fill factor in the y-direction
f_c	Center spatial frequency of grating
f_x	Spatial frequency in the x-direction
f_y	Spatial frequency in the y-direction
f_s	Spatial sampling frequency
$G'(\vec{\rho})$	Fourier transform of filtered Green's function

$G'^{*}(\vec{\rho})$	Complex conjugate of Fourier transform of filtered Green's function
$g'(\vec{r},\vec{\rho}')$	Effective coherent point spread function (filtered Green's function)
$H_A(\vec{\rho})$	Absorption optical transfer function
$H_P(\vec{\rho})$	Phase optical transfer function
$H_P^*(\vec{\rho})$	Complex conjugate of phase optical transfer function
$I(\vec{\rho})$	Intensity function in spatial frequency domain
$I(x,y)$	Image intensity distribution
I_B	Uniform background intensity
$I_\theta(\vec{\rho})$	Intensity function in spatial frequency domain recovered at a single angle
$Im[\quad]$	Imaginary part
i	Unit imaginary number ($\sqrt{-1}$)
k_0	Freespace wavevector magnitude
Λ	Grating period
$\Lambda(y)$	Chirp function
Λ_{pm}	Phase mask period
λ	Freespace wavelength
λ_1	Freespace wavelength for first-order Bragg reflection
λ_m	Freespace wavelength for m^{th}-order Bragg reflection
m	Diffraction order
N	Number of rotation angles
$\mathrm{NA_c}$	Numerical aperture of condenser lens
$\mathrm{NA_o}$	Numerical aperture of objective lens
n	Refractive index

$n(\vec{r})$	Refractive index distribution
$n(y)$	Core refractive index profile
n_0	Average refractive index
$n_0(y)$	Average function of core refractive index profile
n_1	Refractive index modulation amplitude
$n_1(y)$	Apodization function of core refractive index profile
n_{eff}	Effective guided mode refractive index
$n_h(y)$	High-frequency part of core refractive index profile
$\widetilde{n_h}(y)$	Hilbert transform of high-frequency part of core refractive index profile
n_{oil}	Refractive index of oil
$O(n^3)$	Big O notation for upper bound on program runtime with cubic dependence on input size n (not refractive index here)
Ω_z	Measurement domain in the direction of the optical axis
$P(\vec{r})$	Real part of scattering potential (spatial phase function)
$P(\vec{\rho})$	Fourier transform of real part of scattering potential
P_B	Background phase
$\Pi(x, y)$	Two-dimensional rectangular window function
$\Pi(f_x, f_y)$	Modulation transfer function (Fourier transform of two-dimensional rectangular window function)
π	Ratio of circumference to diameter of a circle
ψ_0	Initial phase of core refractive index profile
$\psi(y)$	Unwrapped phase function of core refractive index profile
$Re[\ \ ]$	Real part
$\vec{r}$	Position vector

$\vec{\rho}$	Spatial frequency vector
$\vec{\rho}'$	Wavevector of incident plane wave
$S(\vec{\rho}')$	Intensity distribution at the illumination pupil
θ'	Angle of incidence to Bragg grating
θ_{o}	Maximal half-angle of light entering objective lens
θ_{c}	Maximal half-angle of light exiting condenser lens
u	Integer upsampling factor
w	Integer shifting factor
x	Position along x-axis in selected Cartesian coordinate system
ξ	Cutoff spatial frequency of high-pass filter
y	Position along y-axis in selected Cartesian coordinate system
z	Position along z-axis in selected Cartesian coordinate system
$*$	Convolution

LIST OF ABBREVIATIONS

1D	One-Dimensional
2D	Two-Dimensional
3D	Three-Dimensional
AFM	Atomic Force Microscopy
AOTF	Amplitude Optical Transfer Function
CCD	Charge-Coupled Device
DFT	Discrete Fourier Transform
DIC	Differential Interference Contrast
FBG	Fiber Bragg Grating
FFT	Fast Fourier Transfrom
IR	Infrared
ITDPM	Iterative Tomographic Deconvolution Phase Microscopy
LCI	Low-Coherence Interferometry
LPFG	Long-Period Fiber Grating
MCF	Multi-Core Fiber
MRI	Magnetic Resonance Imaging
MTF	Modulation Transfer Function
NA	Numerical Aperture
NRMSE	Normalized Root-Mean-Square Error
ODT	Optical Diffraction Tomography
OSA	Optical Spectrum Analyzer

OTF	Optical Transfer Function
POTF	Phase Optical Transfer Function
PSF	Point Spread Function
QAM	Quadrature Amplitude Modulation
QPI	Quantitative Phase Imaging
RI	Refractive Index
TDPM	Tomographic Deconvolution Phase Microscopy
TIE	Transport-of-Intensity Equation
UV	Ultraviolet
WOTF	Weak Optical Transfer Function

SUMMARY

The refractive index (RI) characterization of fiber Bragg gratings (FBGs) is crucial in monitoring and validating these fabricated structures. Quantitative phase imaging (QPI) is a uniquely promising candidate to accomplish refractive index characterization with the simultaneous benefits of noninvasive technique, sub-micron resolution, and quantitative 3D recovery of refractive index. Approaches are presented to overcome challenges that have previously acted as major obstacles in this field of research. A form of tomographic deconvolution phase microscopy (TDPM) is used to experimentally demonstrate the characterization abilities QPI can provide for various classes of FBGs.

CHAPTER 1

INTRODUCTION

1.1 Background, Motivation, and Impact

The fiber Bragg grating (FBG) is a crucial structure in the communications and sensing applications of optical fibers. Based on the periodic variation in the refractive index (RI) in the fiber's core, an FBG acts as a narrow optical band-reject filter centered about the first-order Bragg wavelength λ_1, which is two times the effective guided mode refractive index of the fiber, n_{eff}, times the grating period Λ of the RI variation:

$$\lambda_1 = 2n_{\text{eff}}\Lambda \quad (1)$$

For a typical telecommunication wavelength of 1550 nm and typical effective guided mode RI of 1.449, the period of the grating would thus be a mere 535 nm. Practically, a small frequency range is diffracted backwards (reflected) while other optical frequencies are transmitted forward in the fiber. The Bragg grating structure also allows for high-efficiency backward diffraction at higher orders which occur at integer multiples of the optical frequency of first-order diffraction, or equivalently at the first-order Bragg wavelength divided by the order m:

$$\lambda_m = \frac{\lambda_1}{m} \quad (2)$$

This means harmonic frequencies will also be reflected. Some companies fabricate gratings that aim to use second-order diffraction at the wavelength of interest to avoid the difficulties of writing a small grating period. It is common to use an FBG with a grating period of 1070 nm to reflect light at 1550 nm through second-order backward diffraction. It is slightly more difficult to achieve very high reflectivity in a second-order FBG than in a first-order FBG because there may be minor losses through first-order diffraction still occurring simultaneously. Since the first-order diffraction is perpendicular to the propagating mode of the fiber in the ideal case in which second-order diffraction is antiparallel to the incident light (i.e. reflected), it should result in little to no losses. Figure 1 illustrates the diffracted orders in each case.

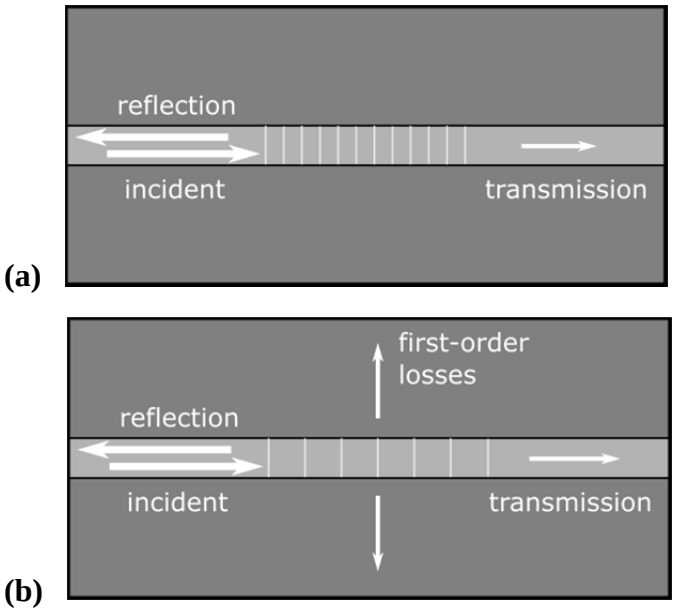

Figure 1. Illustration (not to scale) of backward diffraction at 1550 nm wavelength via (a) first-order diffraction in a 535 nm FBG, and (b) second-order diffraction in a 1070 nm FBG.

FBGs are typically fabricated, or written, in the core of glass optical fibers through exposure to ultraviolet (UV) laser radiation. In some cases, infrared (IR) lasers may be used instead. The most common technique uses a silica glass phase mask, or phase grating, to diffract the light from the laser – pointed at the fiber, perpendicular to the fiber axis – into primarily the +1 and -1 orders before reaching the side of the fiber and photo-imprinting the resulting periodic interference pattern to the core [1-3]. The resulting grating has a period of half the period of the phase mask if at the proper distance [4]. This process is shown in Figure 2.

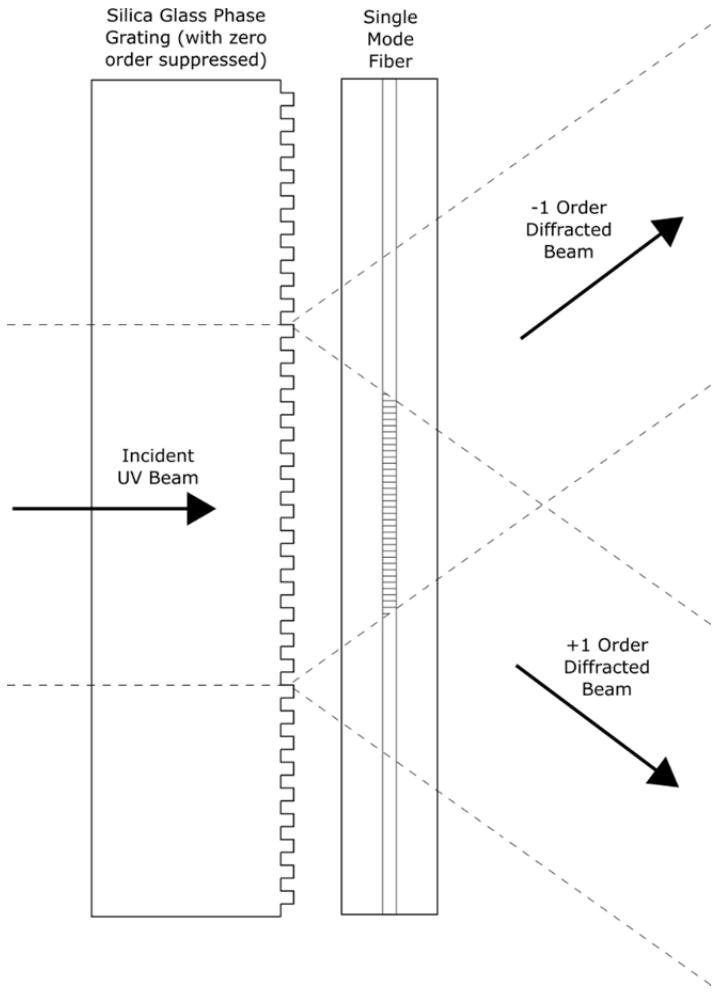

Figure 2. Illustration of phase grating method of photo-imprinting an FBG.

Another important technique is point-by-point writing, in which a laser is translated relative to the fiber along the fiber axis while varying its intensity, whether continuously or in pulses, to induce the desired RI at each point [5, 6]. This is a more difficult but more versatile technique, able to fabricate custom non-uniform axial RI patterns resulting in tailored transmission spectra of the FBG. These techniques can be modified or combined to produce further useful variants of FBGs.

Germania (GeO_2) doping in the core of many fibers is what results in increased RI and makes the core region photosensitive [7]. Different fabrication processes are thought to invoke different structural mechanisms to write the FBGs. Type I, Type I*n*, and Type II are terms to describe fibers written with different variations of photo-imprinting. Type I gratings are written by continuous exposure or by relatively low-energy pulses leading to monotonic increase in RI modulation over exposure time [8]. The mechanism for induced RI change in Type I gratings is thought to be buildup of local electronic defects in the fiber core's structure [9]. If a Type I grating is subject to appropriate additional continuous exposure, the prior RI modulation can be partially erased and slowly rewritten to form a Type I*n* grating through material compaction in the modulated zones of the fiber core [9]. This process results in a negative RI change from the original core RI, whereas the original Type I grating would have a positive RI change due to the initial exposure [10]. A Type II grating is formed from a single high-power pulse from a laser, resulting in a higher maximum possible RI modulation magnitude than other methods, thought to be due to damage to and fusing in the glass structure [9]. Type I*n* and Type II gratings demonstrate much higher temperature stability than Type I gratings [10].

A simple uniform, finite-length FBG with constant-amplitude sinusoidal RI variation results in side lobes in the transmission spectrum [11-13]. These unwanted effects can be mitigated by employing a Gaussian or raised-cosine apodization function in the spatial RI variation profile [14, 15]. The commonly used phase mask writing technique naturally induces some degree of apodization, and this can be further refined in the point-by-point technique. Apodization is the most commonly used non-uniformity in FBGs and is often combined with other kinds of non-uniformities for various applications [16, 17]. Some of these include: 1) tilting, in which the FBG has its fringes oriented off-normal to the fiber axis to allow coupling from a core mode to cladding transmission modes [18-21]; 2) chirping, in which the Bragg wavelength changes throughout the FBG to reflect different wavelengths at different positions in the grating [22-25]; 3) phase-shifting, in which a discrete phase-shift occurs along the grating to create a very narrow transmission resonance and two close reflection peaks in its spectra [26-28]; and 4) sampling, in which an FBG is written over a long-period fiber grating (LPFG) such that the average or center value of the FBG RI variation also varies periodically over a longer length [29-31]. Even with just the common phase mask writing technique for a Type I grating, the average value of the RI varies along the length of the FBG due to the laser's tendency to increase the RI rather than decrease it, resulting in a spatial "average function" that may be similar to a Gaussian or raised-cosine function [32]. These types of non-uniformities are shown in Figure 3. Both the apodization function and average function are important in characterizing an FBG in addition to its Bragg wavelength or chirp function in the case of chirped gratings. Quality factors can also be determined for simple FBGs based on the narrowness of their rejection bands.

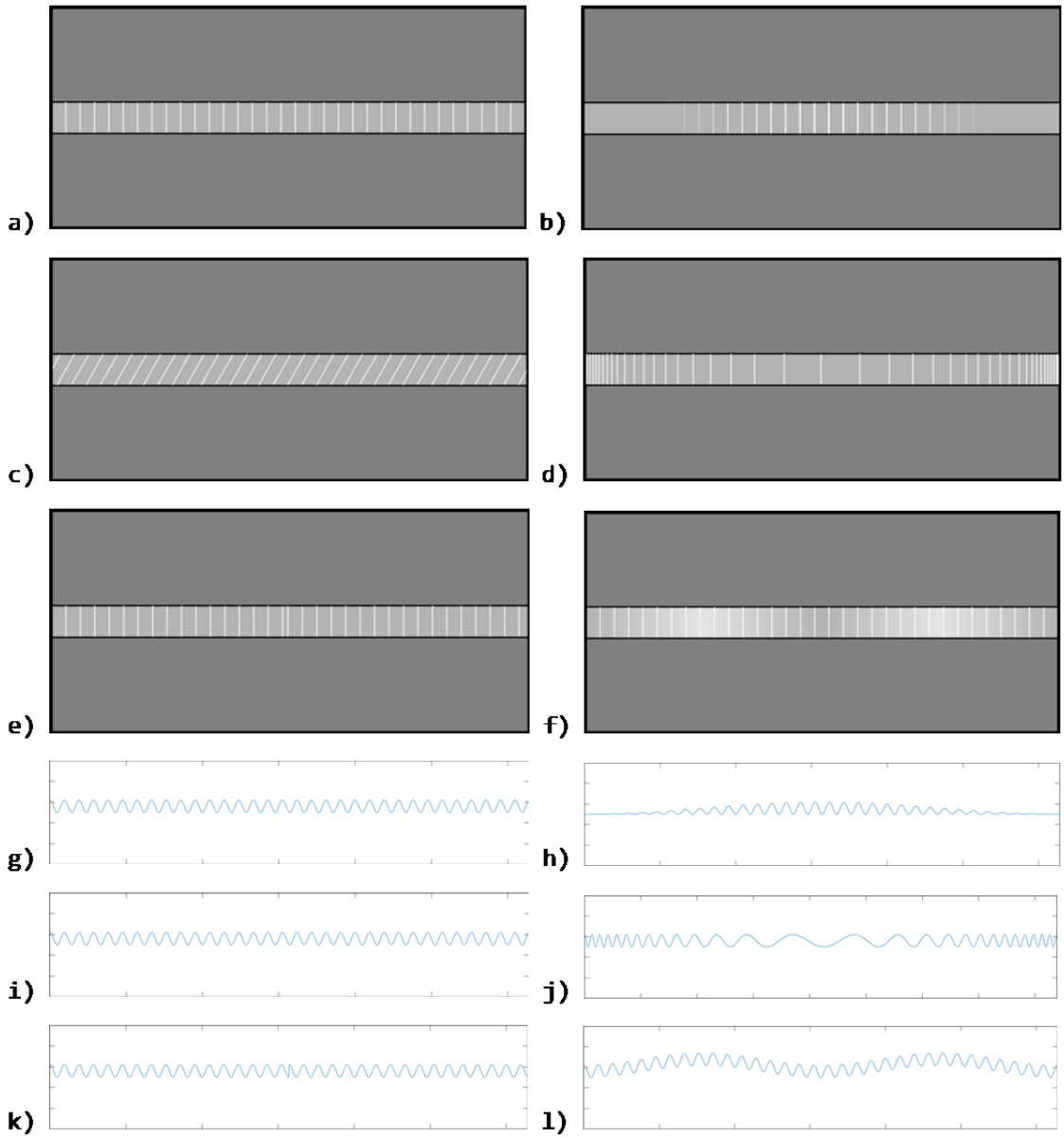

Figure 3. Illustrations (not to scale) of the RI distribution (with lighter color indicating higher RI) of samples of FBGs with (a) uniform RI modulation, (b) apodization, (c) tilting, (d) chirping, (e) phase-shifting, and (f) sampling, along with (g-l) graphs of their respective 1D RI profiles in the fiber core along the fiber axis.

When using fiber for transmitting communications and data, the selective frequency transmission of FBGs can be used for multiplexing and de-multiplexing data [33-36]. Additionally, FBGs in telecommunications may be used for fiber labelling [37] and fault monitoring [38]. FBGs are also used as highly reflective mirrors at their specific Bragg wavelengths, allowing for efficient fiber lasers and fiber resonators [39-41]. Since the Bragg wavelength is affected by temperature [42] and stress [43-45], FBGs are powerful tools in sensing applications as well. Multi-core fibers (MCFs) have recently opened up additional telecommunications bandwidth and sensing capabilities. As their name suggests, MCFs have multiple cores within the fiber all running in parallel along the fiber axis. This allows for even greater multiplexing with the additional spatial channels increasing transmission capacity [46, 47]. FBGs can also be written in MCFs, producing similar communication functions to those in single-core fibers [48-50] and introducing the unique sensing capabilities of the directionality and magnitude of bending in the MCF [51-53]. This powerful shape and position sensing can occur because the Bragg wavelength of each core changes differently due to the different tension and compression required in each core for the fiber to bend in a specified manner. For example, this type of sensor has been instrumental in haptics for minimally invasive surgery [54, 55]. Torsion, or twisting, of the fiber can also be detected using the changes in Bragg wavelengths of the cores [56].

Reflection spectra, being the primary emphasis in fabricating and using FBGs, has been the major focus in characterization of FBGs, even though spectral measurements cannot constitute a full characterization. Increasingly strict manufacturing requirements and more complex variants of FBGs being produced have made correcting for undesired

spectral artifacts effectively a “guess and check” process in the absence of detailed knowledge of the physical RI profile of a fabricated grating. Thus, efficient, accurate, and quantitative RI distribution characterization of FBGs is the approach needed to meet the growing needs of FBG fabrication.

1.2 Literature Review

The one-dimensional (1D) RI distribution can be calculated from the reflection or transmission spectrum using an inverse scattering algorithm such as solving the Gelfand–Levitan–Marchenko equations for the system [57] or using layer peeling approaches [58, 59], but this is only possible if the full complex (amplitude and phase) spectrum is known [60]. It should be noted that the complex reflection and transmission spectra can be very accurately calculated from the RI distribution with the use of coupled mode theory [15]. A complex spectral measurement can be made through low-coherence interferometry (LCI) [61-63] or by frequency-resolved optical-gating [64]. Even so, the resolution of the calculated RI apodization and average functions is usually only about 12-20 μm [61, 62]. A high spatial resolution (small distance resolution) is critical for FBG characterization. If the class of apodization function is known and spectra are collected at two different stress [65] or temperature [66] conditions, a best-fit optimization algorithm can provide the most likely 1D RI profile along the core. However, *a priori* knowledge like this should not be required for an ideal, versatile characterization approach.

Another non-imaging technique to obtain RI distribution data is through side diffraction, which can work in simple circumstances, assuming the RI profile is a grating

such as an FBG [13, 67]. This method uses a beam of coherent light incident transversely to the FBG at the Bragg angle, with the resulting relative zero-order and first-order diffraction strengths corresponding to the magnitude of RI variation in the grating [68], with an RI accuracy of 5×10^{-6} attainable [69]. Using two interfering incident beams can provide even more information if they are properly attenuated and oriented [70]. However, this approach is also significantly resolution-limited, with resolution based on the beam size, which is typically around 10 μm in diameter [68]. Obtaining these sensitive measurements requires extreme precision and is a tedious, complicated process of 1D scanning, making it a limited, inefficient, and ineffective process for FBG characterization.

Standard visible light microscopes struggle to characterize FBGs due to diffraction-limited resolution for visible light being on the same order as the grating period, when accurate characterization from a direct imaging approach requires an even smaller resolution. In addition, a fiber together with its FBG(s) is a phase object, transparent to visible light, so that the only meaningful data contained in the resulting image is the variation in phase of the light that has passed through the fiber, while magnitude remains relatively unchanged and produces little or no contrast. Many conventional imaging techniques rely on magnitude-only approaches, eliminating the possibility of their use in characterizing FBGs.

Differential interference contrast (DIC) microscopy is one optical approach that has been used to perform successful FBG characterization and has even been able to reveal Talbot patterns formed by the grating writing process [8, 9, 71]. DIC uses the recombination of two slightly transversely shifted and orthogonally polarized beams

(split and recombined by Nomarski-modified Wollaston prisms) to optically translate the phase gradient of a two-dimensional (2D) sample into the magnitude of the 2D image formed by the interference of the recombined beams. This creates sufficient contrast for characterization given that the diffraction-limited resolution is also sufficient. Since this is a gradient measurement and information about any magnitude variations is also mixed into the resulting image, this method is inherently qualitative, though some additional conditions and transport-of-intensity equation (TIE) analysis in combination can provide quantitative data [72]. 2D characterization is superior to 1D characterization, but three-dimensional (3D) characterization is desired for completeness and eliminates the concerns for overlapping artifacts, especially with multi-core fibers.

If the cladding of the fiber can be stripped away, this opens up a couple more options for high-resolution imaging, the first of which is atomic force microscopy (AFM) [73]. This type of scanning microscopy uses a miniscule surface probe and measures deflections of a reflected laser beam to obtain a resolution of surface topology measurement that can be less than a nanometer [74]. Writing an RI grating creates a similar "corrugation pattern" [73] in the topology that can be used for some characterization, though the RI is not quantitatively determined in this technique. The cladding typically shows a similar topological pattern to the core, but the core topology can only be known with certainty if the cladding is removed. Another high-resolution technique is near-field imaging, for which the cladding must also be removed. With a detector very close to the core, the high-frequency information is retained in the evanescent field, providing sufficient resolution to characterize an FBG [75, 76]. In any case, however, the stress change in removing the cladding significantly modifies the FBG

through the elasto-optical effect and true characterization cannot be achieved. Thus, a non-invasive approach to FBG characterization is desired. Table 1 summarizes the advantages and disadvantages of the existing characterization approaches presented in this section.

Table 1. Summary of existing RI characterization methods for FBGs.

Method	Non-invasive	High Spatial Resolution	Quantitative	No *A Priori* Knowledge	Control Simplicity	2D Imaging	3D Imaging
Inverse Scattering	☑	☒	☑	☑	☑	☒	☒
Optimization	☑	☒	☑	☒	☒	☒	☒
Side Diffraction	☑	☒	☑	☒	☒	☒	☒
Differential Interference Contrast	☑	☑	☒	☑	☑	☑	☒
Atomic Force Microscopy	☒	☑	☒	☑	☑	☑	☒
Near-Field Imaging	☒	☑	☑	☑	☒	☑	☒

1.3 Research Objectives and Thesis Overview

The immediate objective of the research presented in this thesis is to apply the tomographic deconvolution phase microscopy (TDPM) technique [77] of quantitative phase imaging (QPI) to overcome the aforementioned weaknesses of the current methods of FBG characterization. Specifically, this technique is non-invasive, high-resolution, quantitative, simple to control, 3D, and requires no *a priori* knowledge. TDPM also has the added benefit of not requiring extensive hardware modification to standard Köhler illumination microscopes. Chapter 2 defines and describes quantitative phase imaging and the TDPM methodology proposed, modified, and used in this research.

This immediate objective is attained in two parts – the first of which is solving the challenges that have previously kept TDPM from being used to characterize FBGs. These are, namely, the effects of pixel integration, aliasing, and first-order diffraction within the pupil. In addition, the difficulty of recovering the average and apodization functions must be addressed. The implemented solutions to each of these challenges are discussed in Chapter 3. The second part of accomplishing the overall objective is the experimental collection of data confirming the full characterization of several types of FBGs, including those in MCFs. The procedures and results of the experimentation are included in Chapter 4, and a summary of the research conducted is included in Chapter 5.

Overcoming the previous challenges of using TDPM for FBG characterization identifies the manners in which TDPM is still limited and can be improved, not only for FBG imaging, but also for additional applications such as biological imaging. Specific additional experimentation and FBG imaging is suggested to fortify the data analyzed in this research and to provide additional information with the end goal of improving FBG manufacture and research. This proposed future work is presented in Chapter 5 following the summary of this research.

CHAPTER 2

QUANTITATIVE PHASE IMAGING METHODOLOGY

2.1 Principles of QPI, Tomography, and Deconvolution

QPI is the imaging of the RI values of a phase object using interferometric approaches. QPI is generally non-invasive, high-resolution, and of course quantitative, meeting the needs of an FBG characterization technique. A rapidly developing field, QPI comes in many forms, whether 2D or 3D. 3D QPI typically relies on tomography or deconvolution to assimilate the additional dimension.

Tomography is a method of 3D imaging based on rotation of either the sample or the incident beam relative to the rest of the imaging system to capture a series of 2D phase images for algorithmic reconstruction in 3D. Phase is proportional to the line integral of the RI along the direction of light propagation, allowing for the quantitative recovery of the RI values in 3D. Sample rotation is preferable to beam rotation in some ways, since beam rotation without other parts of the system moving only allows for limited observation angles due to finite numerical apertures (NAs) of the illumination and optical components. It thus leaves a "missing cone" in the spatial frequency domain that can only be filled in using *a priori* knowledge of the sample [78]. Sample rotation is typically used with projection tomography. In sample rotation, the light is assumed to propagate straight through the object, and a 3D image is reconstructed using a filtered back-projection algorithm [79]. Projection tomography does not account for the diffraction and boundary refraction occurring when the sample features are on the same

order as the illumination wavelength, so the line integral used to calculate RI from the phase is a degraded approximation. Optical diffraction tomography (ODT) accounts for these effects to produce a more accurate result, though it requires spatially and temporally coherent illumination, which is subject to coherent noise from sources such as speckle interference and phase jitter [80]. In addition, ODT requires expensive optomechanical equipment.

Providing an alternative or additional technique to tomography, deconvolution is a defocus-based method. Deconvolution uses a through-focal series of images obtained by sweeping the focal plane through and slightly beyond the sample object boundaries along the optical axis, after which the sample RI values can be determined in 3D using a linearized deconvolution model and optical transfer function (OTF) inversion. Phase OTFs (POTFs) relate the defocused images to the phase information. This technique only requires partially coherent (Köhler) illumination and can be accomplished using a standard commercial microscope. The partial spatial coherence provides optical sectioning capabilities when combined with high-NA gating, allowing the system to image objects such as fibers that are thicker than the typical optical system's depth of field by using defocused information [81]. This technique can obtain comparable spatial frequency resolution to that of beam rotation ODT [82]. The downside is that through-focal deconvolution typically results in inherently lower resolution along the optical axis, a challenge when working with complex or fine structures.

TDPM, as described in [77], combines deconvolution and sample rotation tomography to create a methodology both accurate and low-cost due to partially coherent illumination; no laser illumination is required. This combination of techniques enables

thick 3D objects (not just weakly scattering objects) to be imaged in high-resolution. TDPM begins by capturing a through-focal series of bright field images with nonparaxial partially coherent illumination of a sample to form a 3D image which is deconvolved using a 3D POTF – a weak object transfer function (WOTF) in this case, though TDPM has shown to be effective for non-weak thick objects [77] – in accordance with the first Rytov approximation. The first Born approximation is inferior to the first Rytov approximation here since it doesn't hold for thicker samples. The first Rytov approximation is thought to hold provided the RI contrast Δn is small over one wavelength of the illuminating light [79], which is typically the case for FBGs if the surrounding medium, such as oil, has a refractive index close to that of the cladding of the fiber. The sample object is then rotated about an axis perpendicular to the optical axis, and another through-focal series of images is obtained. This process is repeated for multiple angles, up to 180 degrees from the first angle. The information from the deconvolutions at each angle is filtered and combined tomographically to form the final highly accurate 3D RI image.

2.2 RI Recovery with TDPM

The 3D WOTF used in TDPM was first derived from the theory of first-order diffraction tomography in [82] for circular illumination pupils under the paraxial approximation using the first Born approximation. The same form of 3D WOTF was shown to hold with the first Rytov approximation under the additional conditions given by:

$$|A(\vec{r}) * 2iIm[g'(\vec{r},\vec{\rho}')]| \ll 1 \quad (3a)$$

$$|P(\vec{r}) * 2iRe[g'(\vec{r},\vec{\rho}')]| \ll 1 \quad (3b)$$

in which $A(\vec{r})$ and $P(\vec{r})$ are the imaginary and real parts of scattering potential, respectively; $\vec{\rho}'$ is the wave vector of an incident plane wave field; $g'(\vec{r},\vec{\rho}')$ is the effective coherent point spread function (PSF); and $*$ denotes convolution [77]. $A(\vec{r})$ and $P(\vec{r})$ may also be described as the spatial absorption and phase functions, respectively, since they represent the effects of these quantities. This PSF is determined by the Green's function being filtered in the spatial frequency domain to pass forward propagating waves within the circular system pupil. These conditions require weak absorption and slow phase variation, much like the conditions for 2D imaging derived in [83]. If these conditions are met, it is assumed that the Rytov approximation will hold well. Combining these conditions with the assumption of partially coherent illumination, the 3D WOTF is obtained as:

$$I(\vec{\rho}) = I_B\delta(\vec{\rho}) + A(\vec{\rho})H_A(\vec{\rho}) + P(\vec{\rho})H_P(\vec{\rho}) \quad (4a)$$

$$I_B = \int S(\vec{\rho}')\, d\vec{\rho}' \quad (4b)$$

$$H_A(\vec{\rho}) = i\int S(\vec{\rho}')[G'(\vec{\rho}+\vec{\rho}') - G'^*(\vec{\rho}'-\vec{\rho})]\, d\vec{\rho}' \quad (4c)$$

$$H_P(\vec{\rho}) = \int S(\vec{\rho}')[G'(\vec{\rho}+\vec{\rho}') + G'^*(\vec{\rho}'-\vec{\rho})]\, d\vec{\rho}' \quad (4d)$$

in which $\vec{\rho}$ denotes the spatial frequency coordinates related to $\vec{r}$ such that $A(\vec{\rho})$ and $P(\vec{\rho})$ are the Fourier transforms of $A(\vec{r})$ and $P(\vec{r})$, respectively; $S(\vec{\rho}')$ represents the intensity

distribution at the illumination pupil; $G'(\vec{\rho})$ is the filtered Fourier transform of the Green's function, as previously mentioned; I_B is the uniform background intensity (i.e. average image intensity); $H_A(\vec{\rho})$ is the absorption OTF (AOTF); and $H_P(\vec{\rho})$ is the POTF to be used for TDPM [77]. In preparing to capture an image in TDPM, a 2D Gaussian distribution for $S(\vec{\rho}')$ is assumed and obtained by applying a best-fit curve to an image obtained of the back focal plane of the objective lens.

Rotation of 360 degrees allows for obtaining $P(\vec{r})$ by subtraction of the opposite images in the same coordinate system due to symmetry of the 3D WOTF and the absorption contrast function being even about each scattering point. This is additionally helpful since all even terms in the Taylor expansion of the intensity function produce even contrast, so strong pure phase objects can be better imaged. However, rotation of 180 degrees is sufficient for pure phase objects, and that is the method used for this experiment. The object must be rotated N times at evenly spaced angles between 0 and 180 degrees, inclusive, where $N \geq \frac{\pi}{\theta_c}$ [77]. The marginal illumination angle expressed in radians as θ_c is defined as $\theta_c = \sin^{-1}\left(\frac{\mathrm{NA_c}}{n_0}\right)$, with $\mathrm{NA_c}$ being the NA of the condenser lens and n_0 being the average RI. It is often necessary to use a higher N than this minimum value to ensure sufficient contrast through all spatial frequencies.

A formal least-squares approach can be used to solve directly for the real part of scattering potential (absorption effects are ignored in TDPM for phase objects):

$$P(\vec{\rho}) = \frac{\sum_{j=0}^{N-1}\left[\frac{I_{\theta_j}(\vec{\rho})}{I_B}\right]H_P^*(\vec{\rho})}{\sum_{j=0}^{N-1}\left|H_{P_j}(\vec{\rho})\right|^2+\alpha} \quad (5)$$

The scattering potential is then translated into RI. When capturing the images, multiple images are usually captured and averaged at each step of the through-focal series to remove noise. The measurement domain of the series should encompass the entire object of interest and extend further to encompass scattered intensity variations, ensuring there is sufficient spatial frequency resolution for reconstruction without aliasing. Typically, not all scattered intensity variations can be captured in the measurement domain, which reduces the low-frequency contrast, so a separate low-frequency algorithm is required for reconstruction. Thus, TDPM traditionally applies separate algorithms on the low-frequency and high-frequency components.

Before both algorithms are applied, the images undergo preprocessing, beginning with normalization of background intensity. An additional through-focal series without the sample object present is collected and used to subtract out other intensity variations in the system. The 3D images are then up-sampled along the optical axis of the system if necessary so that the scaling matches the lateral resolution. Finally, the images are shifted to a single center rotation axis of best correlation through as registration procedure.

The high-frequency RI recovery algorithm used in TDPM numerically calculates the least-squares solution. It first filters each through-focal series in the frequency domain with the conjugate of the POTF. Each series is then rotated to account for the sample object's physical rotation angle using bilinear interpolation in the real space domain before they are all summed. This resulting sum is then filtered with the denominator portion of Equation (5), which accounts for the overlapping of frequency domain coverage among rotation angles, and a high pass filter with a hard cutoff at $\xi = \frac{1}{\Omega_z \sin \theta_c}$,

where Ω_z is the measurement domain in the direction of the optical axis [77]. This gives the scattering potential, which is then converted to RI:

$$n(\vec{r}) = \sqrt{\frac{P(\vec{r}) - P_B}{k_0^2} + n_0^2} \quad (6)$$

in which k_0 is the freespace wave vector magnitude for the illuminating light and P_B is the background phase. Frequencies below ξ typically cannot be recovered accurately due to insufficient frequency resolution and not fully encompassing the scattering intensity, as already mentioned.

The low-frequency algorithm used in TDPM for frequencies below ξ is based on traditional filtered back-projection but incorporates the assumptions of partially coherent illumination. After preprocessing, the phase is recovered for each 2D z-slice of each through-focal series using a method with the ability to model partial coherence. This could be TIE phase recovery [84], inversion of the 2D WOTF [85], or 2D POTF recovery [86], which was chosen by Jenkins in [77] and is used in the experiments for this thesis. Generally, with partially coherent illumination of a phase object in 3D, depth-resolved phase recovery will not provide valid results because the out-of-focus planes carry no meaning in their phase, but with the constraint that frequency is below ξ, the conditions for use are justifiably met in that the z-slice phase and the measurement plane are largely independent. The rest of the algorithm mirrors conventional back-projection. Since the sampling density is greatest near the frequency origin, the phases obtained are filtered using cylindrically symmetric normalized Ram-Lak filters [87]. Each through-focal series

is rotated using bilinear interpolation and summed. A low-pass filter with a hard cutoff at ξ is applied, and then the scattering potential is converted to RI with a level shift, since this algorithm does not use absolute phase information:

$$n(\vec{r}) = \Delta n(\vec{r}) + n_{\text{oil}} \quad (7)$$

where Δn is the RI variation computed from the fiber images and n_{oil} is the refractive index of the surrounding oil medium used as a reference. The resulting RI distributions obtained from the low-frequency and high-frequency algorithms are combined to create the final overall RI image. Jenkins [77] illustrates this process with a block diagram shown in Figure 4.

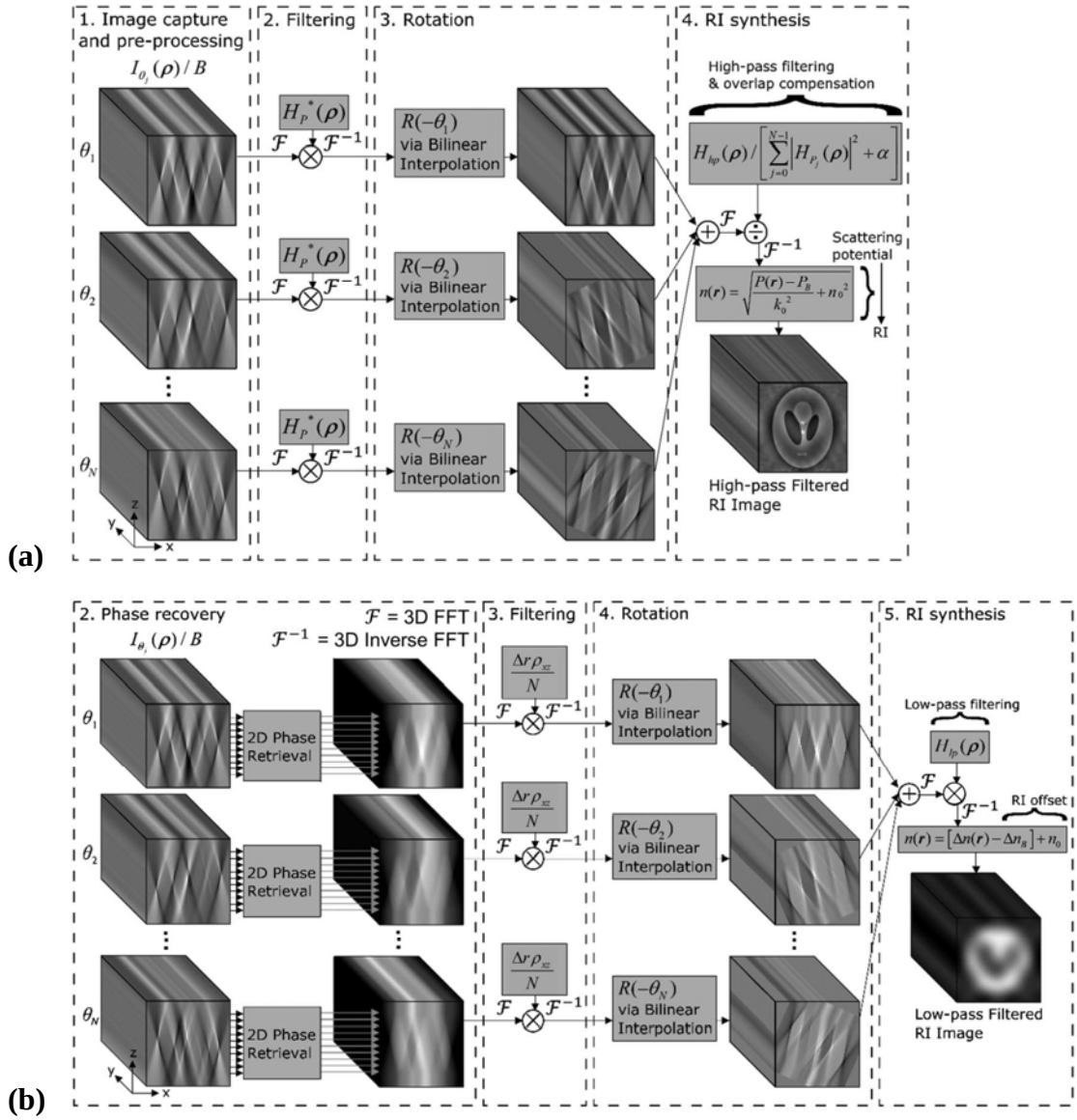

Figure 4. Block diagram representation of TDPM RI recovery for (a) high frequencies and (b) low frequencies. (Reprinted with permission from [77], The Optical Society)

CHAPTER 3

CHALLENGES AND SOLUTIONS

3.1 Pixel Integration Effect

In the following discussions, the effective camera resolution is denoted as Δy. Since a microscope is used, this quantity is the actual camera resolution divided by the microscope magnification factor. This is equivalent to the effective pixel spacing.

When using a camera for measurement, the continuous analog intensity function $I(x, y)$ of the real image that is cast onto the sensor is discretized and digitized by the individual sensor pixels. The pixels do not simply sample the image intensity, however, but calculate the average intensity over the rectangular pixel area; this is the pixel integration effect [88]. Since FBGs have such short periods, this presents a challenge.

This effect can be modeled as a convolution with the 2D rectangular window function $\Pi(x, y)$ which represents the sensor pixel area [88]. In the spatial frequency domain, this translates to a multiplication by $\Pi(f_x, f_y) = \frac{\sin(\pi f_x \mathrm{FF}_x \Delta x)}{\pi f_x \mathrm{FF}_x \Delta x} \frac{\sin(\pi f_y \mathrm{FF}_y \Delta y)}{\pi f_y \mathrm{FF}_y \Delta y}$, commonly called the modulation transfer function (MTF) [89]. Here, FF specifies the 1D fill factor in the direction of its subscript. The fill factor is the ratio of the pixel size in that direction to the pixel spacing in that direction since there is some "empty" space between pixels. Therefore, $\mathrm{FF}_y \Delta y$ specifies the pixel size in the y-direction. Let the y-direction be the direction of the grating. This makes it such that there is almost no high-frequency component to the variation in the x-direction. The y-direction, containing the grating variation, should show relatively high intensity in the spatial frequency domain at

$\frac{1}{\Lambda}$. The pixel MTF can be approximated to be unity for low frequencies near zero (DC component) and $\frac{\sin(\pi f_y \mathrm{FF}_y \Delta y)}{\pi f_y \mathrm{FF}_y \Delta y}$ for higher frequencies (AC component).

Analysis of this approximation reveals that if the period of an AC component of the image intensity along the y-direction (such as the period of the grating) is near the y-length of a sensor pixel, that component will be attenuated or even removed in the digitization process. Thus, the camera hardware must have sensor pixels adequately sized to pass such frequencies. When processing the images, the AC component should be isolated (through simple frequency filtering) and divided by the simplified MTF approximation for AC to account for the pixel integration effect.

3.2 Aliasing Effect

An ideal RI grating has the form $n(y) = n_0 + n_1 \cos(2\pi\, y/\Lambda + \psi)$, with a constant background average component and sinusoidal component. Thus, the spectrum would consist of three delta functions at 0 and $\pm f_c = \frac{1}{\Lambda}$. Physical gratings do not exhibit infinitely narrow delta functions in spectra since they are not infinitely long and both $n_0(y)$ and $n_1(y)$ vary along the length of the grating, the former being the average function and the latter being the apodization function. Even so, the main structure of the intensity spectra of simple FBGs typically consists of three relatively narrow bands at the aforementioned spatial frequencies.

By the Nyquist criterion, full information about an object generally cannot be recovered if the sampling resolution, or camera resolution Δy in this case, is larger than

$\frac{1}{2f_c} = \frac{\Lambda}{2}$ [90]. However, even if aliased, the three bands can be distinguished in some cases such that the pertinent information can be recovered using bandpass sampling [91, 92]. The high frequency bands can be shifted to the baseband such that they do not overlap if the quantity $\frac{\Delta y}{\Lambda}$ is less than 1.0 and is sufficiently far from 1.0 and 0.5. Bandpass signals with bandwidth B and center frequency f_c can achieve lossless recovery if the sampling rate $f_s = \frac{1}{\Delta y}$ meets the following criterion:

$$\frac{2f_c+B}{w+1} \leq f_s \leq \frac{2f_c-B}{w} \quad (8)$$

where w is an integer such that $0 \leq w \leq \frac{2f_c-B}{2B}$. This ensures the two aliased bands do not overlap, and they can be effectively restored to their correct positions in preparation for QPI processing at the correct frequency. With the case of the zero-frequency band being present, however, further restrictions are imposed on f_s to be certain the high frequency bands are sufficiently distinguishable from the zero-frequency band. Namely, f_s must be sufficiently far from its bounds defined in Equation (8).

Additionally, since the QPI algorithm must be applied to the appropriate frequency components, the recorded data must first be upsampled by an integer factor u such that the new effective pixel spacing $\delta y = \frac{\Delta y}{u} < \frac{\Lambda}{2}$. This allows full recovery of the data in the absence of noise. Then the shifting index w will be equal to $\frac{\Delta y}{\Lambda}$ rounded to the nearest integer so that each band is shifted by wf_s. If rounded down, the right band shifts right and the left band shifts left. If rounded up, the left and right bands switch relative positions, with the right band shifting left and the left band shifting right. If the

bandwidth of each band is at most $\frac{f_s}{3}$, then the average and apodization functions can be recovered with a resolution of $3\Delta y$.

3.3 First-Order Diffraction within the Pupil Effect

The objective lens' numerical aperture must be large enough to capture and include the first-order diffracted light, which holds key information about the periodicity, from the FBG sample. In the case of normal plane wave illumination, the numerical aperture of the objective lens must be larger than the ratio of the wavelength to the grating period. However, since TDPM uses only partially coherent illumination, the requirements are less strict. The illumination comes from an extended source, provided by the condenser lens, allowing for a range of incident angles illuminating the sample, some of which will have first-order diffraction into the objective lens even if normal incident light does not. The effective requirement in this case is then $\mathrm{NA_o} + \mathrm{NA_c} > \frac{\lambda}{\Lambda}$. The numerical aperture of both lenses and the illumination wavelength must be carefully selected with this requirement in mind.

3.4 Recovering the Characteristic Functions

The one-dimensional RI distribution in the core along the FBG can be represented by the equation $n(y) = n_0(y) + n_1(y)\cos(2\pi\, y/\Lambda + \psi_0)$, where $n_0(y)$ is the average function, describing how the center RI about which the modulation occurs may gradually change over the length of the grating; $n_1(y)$ is the apodization function, describing how

the amplitude of the periodic modulation changes throughout the length of the grating. Demodulation signal processing techniques can recover these functions from the point-by-point RI distribution [93]. The first and second terms can be separated by simple filtering to isolate $n_0(y)$.

The Hilbert transform can be used to put the high-frequency component $n_h(y) = n_1(y)\cos(2\pi\, y/\Lambda + \psi_0)$ in an analytic form $\widetilde{n_h}(y) = n_1(y)e^{i(2\pi y/\Lambda+\psi_0)}$. The magnitude of the result is the apodization function, and the phase of the result is related to the period of RI modulation. For chirped gratings, the local period varies along the length of the grating as a function $\Lambda(y)$. In this case, $\Lambda(y)$ is called the chirp function. The chirp function can be recovered from the phase of the Hilbert transform once it is unwrapped [94]. The chirp function can be recovered from the unwrapped phase function $\psi(y)$ according to the equation $\Lambda(y) = \frac{2\pi}{\frac{d}{dy}(\psi(y))}$, since $\frac{d}{dy}\big(\psi(y)\big)$ gives the instantaneous spatial frequency. The chirp function cannot be recovered using this method if a discrete phase shift occurs in an FBG, but if the RI distribution clearly reveals where the discrete phase shift occurs, the FBG can be treated as two distinct FBGs for recovery of characteristic functions, which may then be joined at the location of the phase shift. The average function, apodization function, and chirp function make up the characteristic functions of an FBG, which can be recovered from the RI distribution data along the center of the fiber core in which the FBG is present.

For unchirped gratings, the high-frequency component $n_h(y)$ can be treated as analog quadrature amplitude modulation (QAM) to recover the apodization function without the use of the Hilbert transform [95].

Bao [94] combines the TDPM process as described in [77] with the challenges described above to form a complete proposed procedure for image processing for FBG characterization, shown as a flowchart in Figure 5. Note that this figure assumes the grating is in the x-direction, and a simple substitution of y for each x will yield the equivalent process for the coordinate system of this research.

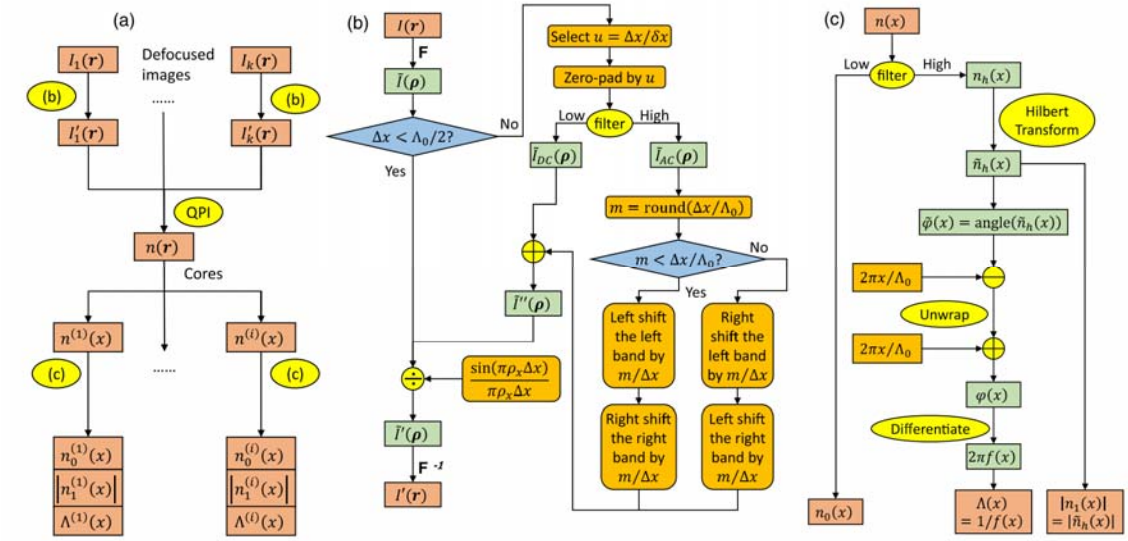

Figure 5. Flowchart showing the basic procedure of characterizing FBGs using QPI. (a) The overall flowchart, which calls sub-flowcharts (b) and (c). The QPI algorithm can be any appropriate method in the literature. (b) Sub-flowchart for processing the defocused images, including the compensation for the pixel integration effect and the necessary upsampling. (c) Sub-flowchart to recover the average RI, the apodization function, and the local period for a given line RI profile in an FBG. (Reprinted with permission from [94], The Optical Society)

This process is generalized for multiple FBGs in MCFs. This process is also abstracted such that the QPI step can be accomplished by techniques other than TDPM, such as phase-shifting holography [96] or solving transport-of-intensity equations to recover the refractive index distribution.

CHAPTER 4

EXPERIMENTAL CHARACTERIZATION OF FIBER BRAGG GRATINGS

4.1 Prior Simulations

This work directly extends the work done by Bao in improving and simulating TDPM techniques for FBG imaging [94]. Considering the same challenges from Chapter 3, Bao was able to successfully recover the characteristic functions of simulated FBGs in various simulated single-core and multi-core fibers subject to the same conditions and TDPM methodology as that employed in this work [94]. The most complicated simulation example from Bao's work is shown in Figure 6.

Among the four FBGs simulated here, the average normalized root-mean-square error (NRMSE) values along the center-of-core line profiles were around 0.042 for the recovered apodization functions and 0.055 for the recovered average functions [94]. The resolution of these recovered functions was approximately 1 micron, sufficient for characterizing almost any continuous real FBG. It should be noted that 1 micron is not sufficient resolution in the raw RI distribution for characterization, but for the characteristic functions calculated from the RI distribution, this scale of resolution is more than enough for reasonable rates of change in a physical sample.

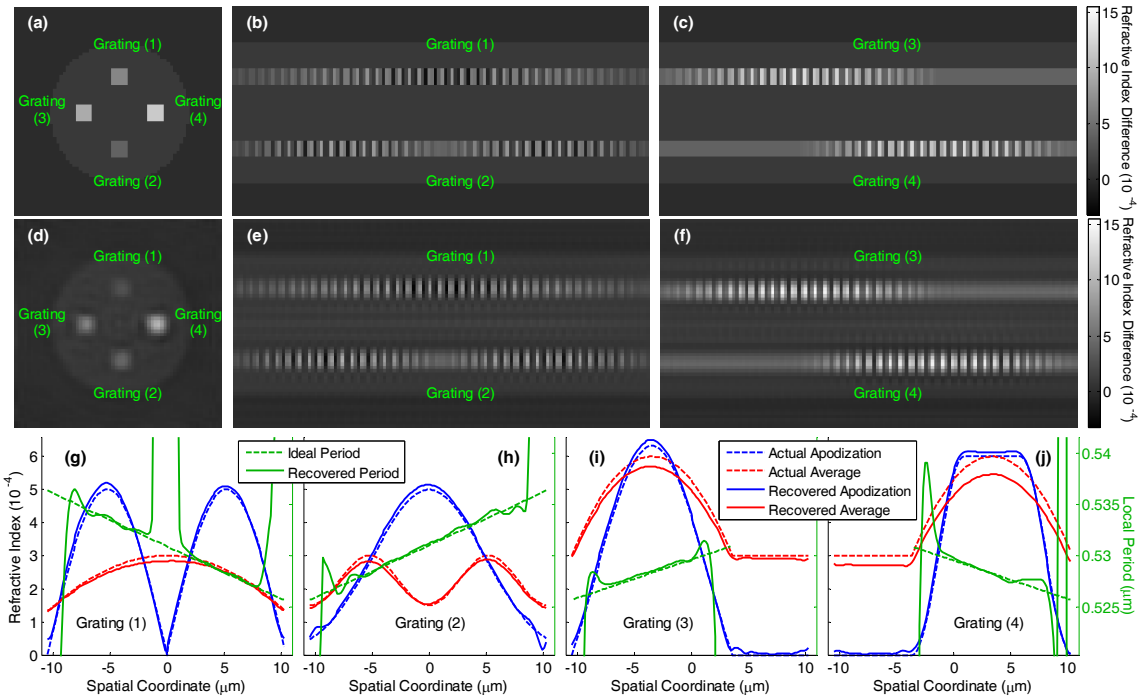

Figure 6. Simulation results of RI difference in a four-core fiber with each core containing an FBG. (a)-(c) The three orthogonal center cross sections of the original simulated object. (d)-(f) The three orthogonal center cross sections of the recovered RI. (g)-(j) The actual (dashed) and reconstructed (solid) characteristic functions, including average (red), apodization (blue), and chirp (green) functions, in the center of the four FBGs. (Reprinted with permission from [94], The Optical Society)

4.2 Experimental Configuration

The microscope used is an Olympus BX60. An Olympus BH2-RFL-T2 mercury lamp is the illumination source. The camera in use is a Q-Imaging Retiga 1300R. The Physik Instrumente P-721SL2 is a piezoelectric device used to scan the objective lens along the imaging system's optical axis to precisely adjust the focal plane for collecting the through-focal series of images. A Newport Universal Motion Controller ESP 300 is used with stepper motors to rotate the fiber. Various FBGs are imaged, but all are in SMF-28 fiber [97]. SMF-28 fiber has a core diameter of 8.2 μm and a cladding diameter

of 125 μm. Many SMF-28 fibers also have a layer of acrylate coating outside the cladding with a diameter of around 242 μm, which is stripped and removed from the region of the fiber containing the FBG of interest prior to imaging such that only core and cladding are imaged. The fiber core of unperturbed SMF-28 fiber has a typical refractive index of 1.462. Each FBG imaged is designed to reflect at a center wavelength of about 1550 nm.

The procedure followed in this experiment closely follows that developed by Jenkins in [77] and that analyzed and simulated by Bao in [94]. This experiment does, however, make a slight change to the physical setup from previous TDPM configurations for imaging fibers. Previously, in TDPM and similar fiber imaging experiments [98], the fiber coating was stripped from one end of the fiber to reveal a region to be imaged, and the unstripped end was inserted into a rotation stage controlled by a stepper motor. Having only one end of the fiber clamped by a rotation stage allows the fiber to bend and have some "slack" between the imaged portion and the rotation stage. The motion produced by rotation of the fiber may slightly add to or decrease the amount of "slack" in the fiber, consequently shifting the part of the fiber in the image field of view along the fiber axis. This is acceptable for fiber with very low RI variation along the fiber axis, but for an FBG, even shifts in the tens of nanometers between angles of image collection can produce significant error in the resulting refractive index distribution. If the shifting of the fiber along the fiber axis between consecutive angles can be limited to strictly less than half the FBG period for a simple FBG, a best-fit correlation algorithm can realign the images in processing.

This half-period limit cannot be guaranteed with a single clamp location, so for these experiments, a second clamp location and second synchronous stepper motor are added on the other end of the fiber to eliminate "slack." The fiber will thus experience a small tensile force along the fiber axis. As little tension as possible should be applied while still eliminating "slack" so that the photoelastic effect does not result in any significant changes in the FBG's RI from its unstressed state. The strain and change in length of the fiber must be effectively zero so the grating period remains unchanged. To ensure structural stability of the fiber, the acrylate coating should remain on both regions to be clamped, so the coating is only stripped in the middle of the fiber where the images will be captured. This modified setup also requires that the rotation stages be precisely positioned such that the line connecting their centers (and the axis of rotation) lies in the center focal plane for the through-focal series and passes through the optical axis of the imaging system (or equivalently, the center of the field of the view). Even with this dual rotation stage providing dramatic improvement, a shift of more than half the period of the grating commonly occurs during rotation and adjustment in the present system configuration. This remains a challenge to be adequately addressed and poses a serious issue for FBG measurement because any unregistered shift, when back-projected, can cancel some or even all of the modulation amplitude since the grating images are out of phase with each other between angles.

The system configuration for this experiment is shown in Figure 7 and shows the dual rotation stage as described at label number 5.

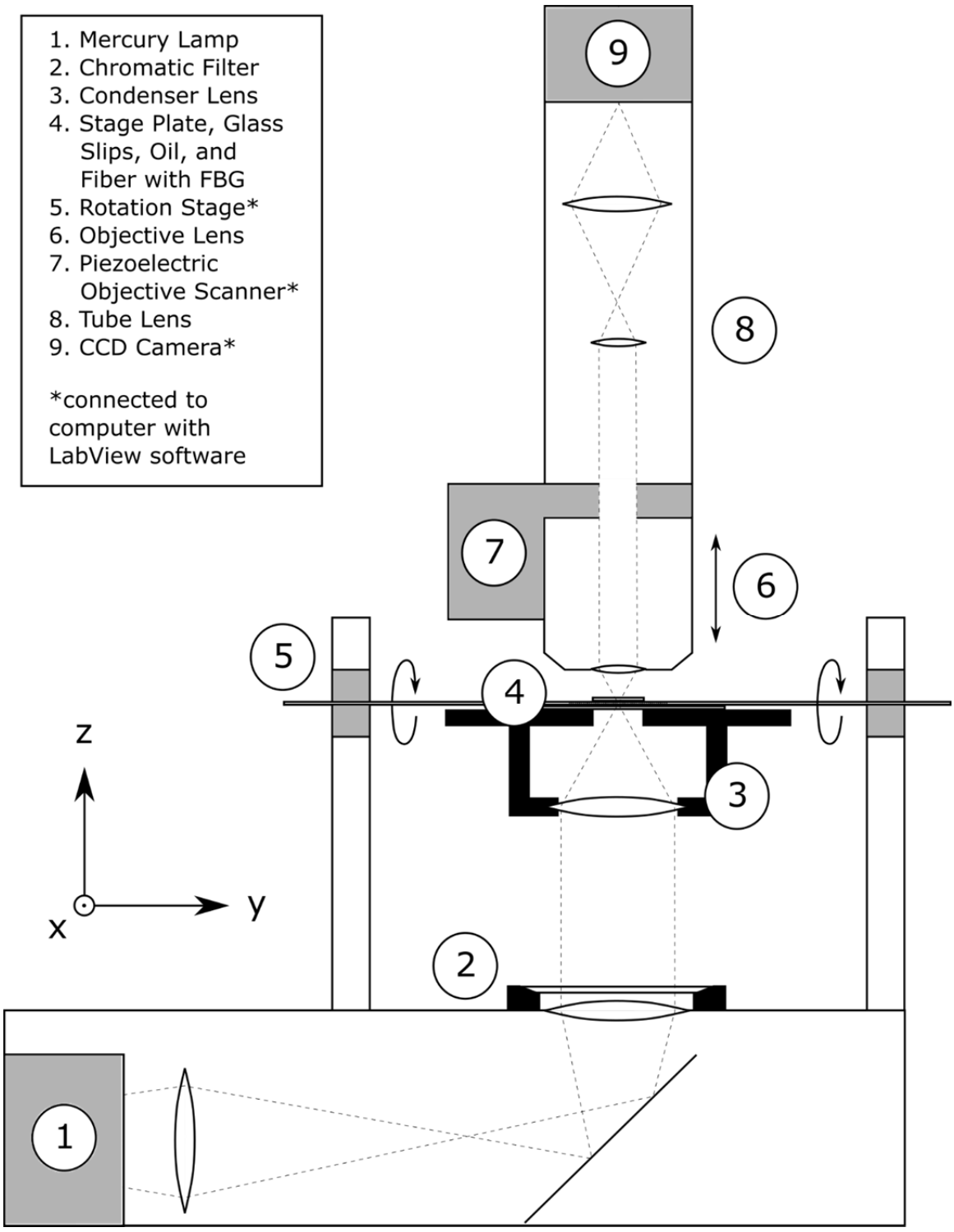

Figure 7. Cross sectional diagram of experimental system configuration.

In this experiment, the three-axis Cartesian coordinate system is defined relative to the fiber and thus rotates as the fiber rotates. The z-axis is defined by being parallel to the optical axis of the imaging system when the first through-focal series is collected (when the rotation angle is zero). The y-axis is defined by being parallel to the fiber axis. The x-axis is perpendicular to the y and z axes. The origin of the coordinate system is arbitrary for most purposes, but it is selected to be the corner of the 3D region being reconstructed such that the resulting RI distribution is determined entirely in the first octant of the coordinate system (all x, y, and z values are positive for the determined RI data).

The light propagation path for this system begins at the mercury lamp denoted by label number 1 in Figure 7. The light is then aligned with the optical axis of the microscope imaging system, collimated, and filtered to pass light at a narrow band of wavelengths centered at 546 nm, as shown at label number 2 in Figure 7. The condenser lens at label number 3 in Figure 7 provides Köhler illumination to the fiber sample plane, and the objective lens at label number 6 in Figure 7 collimates the light from the desired focal plane. Finally, the tube lens at label number 8 in Figure 7 and additional optical components are used to focus the light to form an image on a charge-coupled device (CCD) camera, as shown at label number 9 in Figure 7. The recorded image data is then transmitted to a computer to be saved for later processing. The exposure time for each image should be adjusted so that the maximum pixel intensity is well below the maximum allowed intensity so that no clipping occurs. As long as significant headroom exists to avoid clipping, a longer exposure time provides better noise performance and contrast, which is preferred.

As shown at label number 4 in Figure 7, the stage plate has a hollow center to allow light to pass through. This hollow center region is covered by a glass slide which the fiber rests on. Two thin slips of cover glass (not shown in Figure 7) are placed on either side of the fiber, also resting on top of the glass slide. These slips should have a thickness slightly greater than the diameter of the fiber cladding. Index matching oil is then added between the slips of cover glass to completely envelop the fiber in the region where imaging will take place. The index should be slightly different from the fiber cladding so that registration of the fiber position can occur. The boundaries between the oil and cladding produce slight contrast in defocused images that allows the images to be aligned before any other processing is done. Shifting pixels in the image such that these boundaries match those of a simulated fiber in a certain refractive index of oil ensures the fiber is centered and oriented such that the fiber axis points exactly along the pixels in the y direction of each the image. This is crucial in being able to reconstruct a cohesive 3D RI distribution from the 2D images. However, this pixel shifting can introduce error if the fiber is at a significant angle from the desired fiber axis direction. The CCD camera shown in Figure 7 can be rotated freely about the optical axis of the imaging system, so that if the user aligns the camera properly, this is not a significant concern. Additionally. This kind of alignment, or registration, does not fix issues with the fiber shifting along the fiber axis between rotation angles as previously discussed.

For this experiment, an oil with a nominal RI of 1.460 is used to provide some contrast to the fiber cladding with an RI of around 1.458. A final glass cover slip (shown in Fig. 6) is placed on top of the region of fiber to be imaged such that it rests on top of the other two slips of cover glass and creates an effectively flat top to the body of oil with

no air bubbles. Since each glass or oil layer the light passes through is effectively flat and of constant RI, zero phase difference and thus zero contrast will occur due to these layers. This allows the fiber alone to be imaged accurately. Once this setup is prepared, the illuminating light should be left on exactly as it will be used for imaging for a few hours prior to data collection. This will allow the thermal effects to settle such that negligible change in refractive index, stress, and shape will occur during imaging in any part of the setup.

Figure 8 is a photograph of the experimental system configuration to give a sense of scale.

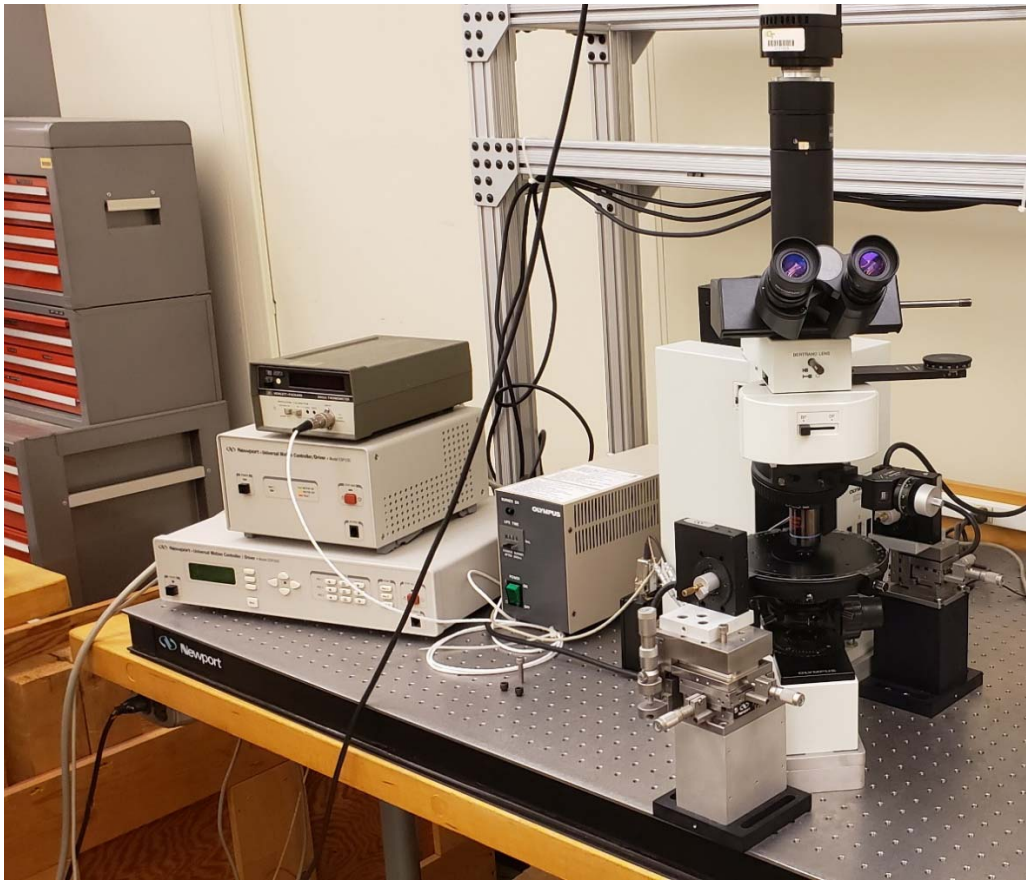

Figure 8. Photograph of experimental system configuration.

4.3 Experimental Parameters

Using the configuration with the 50X objective lens in place, a reference scale with length of 250 μm was found to correspond to a 1278-pixel length along the y-axis, so the effective pixel spacing Δy is 196 nm. This corresponds to an effective sampling rate of $f_s = \frac{1}{196\text{ nm}} = 5.102\ \mu\text{m}^{-1}$. Since the effective pixel spacing is less than half the grating period (and equivalently, the spatial sampling frequency is more than twice the spatial frequency of the grating), the Nyquist criterion is met, and no upsampling is required ($u = 1, w = 0$). However, if upsampling and aliasing correction were required for this experiment, this pixel spacing would be the Δy value used for such processing.

The Retiga 1300R image sensor has a manufacturer-specified 1D pixel spacing of 7.4 μm [99]. This was confirmed through direct microscopic measurement of the pixel sensors. This means that with the other optics in the system (including the tube lens), the effective overall objective-tube system magnification is only 37.7X to achieve an effective pixel size of 196 nm. A reduction in magnification compared to the nominal objective magnification is consistent with other infinity-corrected optical systems [100]. For these analyses, only the effective pixel spacing and effective pixel size (accounting for magnification) are considered.

During confirmation of the pixel spacing, the 1D fill factor was also computed to be $\text{FF}_x = \text{FF}_y = 78\%$. This specification is not advertised for the camera. The effective pixel size for the pixel integration effect is thus 153 nm. This value of $\text{FF}_y \Delta y$ is used in the MTF: $\frac{\sin(\pi f_y \text{FF}_y \Delta y)}{\pi f_y \text{FF}_y \Delta y}$. Since the period of a first-order Bragg diffraction grating (for reflection of 1550 nm light) is approximately 535 nm, the spatial frequency of the grating

is $f_y = \frac{1}{\Lambda} = \frac{1}{535\text{ nm}} = 1.869\ \mu\text{m}^{-1}$. Thus, the MTF at the grating frequency is $\frac{\sin[\pi\cdot(1.869\ \mu\text{m}^{-1})\cdot(153\text{ nm})]}{\pi\cdot(1.869\ \mu\text{m}^{-1})\cdot(153\text{ nm})} = 0.871$. For a second-order grating with period of approximately 1070 nm, the MTF is 0.967.

An objective lens having a numerical aperture of 0.75 is used. A condenser lens of adjustable numerical aperture is used, and a numerical aperture of 0.50 is selected. A chromatic filter is applied to pass only a narrow band of the mercury lamp's illuminating light at a center wavelength of 546 nm. Thus, the first-order diffracted light from the FBG is captured for analysis, since $\text{NA}_\text{o} + \text{NA}_\text{c} = 1.25 > \lambda/\Lambda = \frac{546\text{ nm}}{535\text{ nm}} = 1.02$.

In recovering the chirp function of an FBG, a first-order Savitzky-Golay differentiation filter with a frame length of 30 is used to estimate the derivative of the phase of the FBG's periodic variation [101].

The maximum angle allowed between through-focal series is $\theta_\text{c} = \sin^{-1}\left(\frac{\text{NA}_\text{c}}{n_0}\right) = \sin^{-1}\left(\frac{0.5}{1.46}\right) = 20$ degrees, corresponding to a minimum N value of 9. $N = 15$ rotation angles are used so that the angle of rotation between series is 12 degrees to ensure sufficient contrast at all spatial frequencies of interest and alleviate the missing cone problem. Each through-focal series consists of an image at each of 731 positions of the piezo scan, with 5 images captured and averaged at each position to reduce noise. The spacing between objective scan positions is 134 nm in air, corresponding to a spacing between focal plane scan positions within in the oil medium of 196 nm (due to refraction) such that the resolution along the optical axis equals the transverse resolution. This means each series spans a region measuring 143 μm along the system's optical axis, enclosing the fiber cladding and slightly beyond.

Multiple methods of calculating the 3D PSF for TDPM have been performed, the first of which assumes a flat disk illumination profile, for which the PSF can be quickly analytically determined, but this produces inaccurate results since the experimental illumination profile is Gaussian. The split-step beam propagation method [102] was later used to simulate the 3D PSF with high accuracy, but the computation time for this approach can be on the order of a month with current hardware. In this research, a new approach is used in which the 2D POTF of a Gaussian profile is determined semi-analytically as described in an appendix of [103], and this 2D POTF is then rotated about its center (because of illumination symmetry) to allow for calculation of the 3D PSF. This approach to calculating the 3D PSF has a computation time of just a few minutes on current hardware, similar to that of analytical determination with the flat disk illumination assumption. This new approach is also able to achieve results that appear to be at the same level of accuracy as those provided by the split-step beam propagation simulated PSF. The PSF resulting from this method produces aliased off-center copies of the desired PSF, so the resulting PSF is cropped to isolate the intended portion of the function and recover clean results.

The low-frequency portion of the TDPM algorithm outlined in Figure 4(b) is not used for this research, as the high-frequency algorithm outlined in Figure 4(a) was found to produce cleaner results across all frequencies for fiber imaging. Effectively, the cutoff frequency ξ introduced in Chapter 2 is reduced to zero.

4.4 Experimental Results

4.4.1 Specifications of FBGs Imaged

The four FBGs imaged in this research span a variety of manufacturing techniques and specifications, given by the manufacturers as detailed in Table 2.

Table 2. Specification summary of FBGs imaged.

	FBG 1	FBG 2	FBG 3	FBG 4
Manufacturer	Technica Optical Components [104]	Technica Optical Components [104]	FemtoFiberTec GmbH [105]	FemtoFiberTec GmbH [105]
Model Number	T10	T70	FFT.FBG.S.00.02	FFT.FBG.S.00.03
Writing Technique	Phase Mask	Phase Mask	Point-by-Point	Point-by-Point
Grating Type	Type I	Type I	Type II	Type II
Nonlinearity	Apodized	Chirped and Apodized	Apodized	Apodized
Center Wavelength	1550.31 nm	1550.02 nm	1549.97	1549.95 nm
Reflectivity	99.999%	99.978%	65.3%	75.6%
3-dB Bandwidth	1.18 nm	12.20 nm	0.46 nm	0.25 nm
Length	10 mm	10 mm	3.1 mm	5.9 mm
Fiber Type	SMF-28e+	SMF-28e+	SMF-28e+	SMF-28 Ultra

FBG 1 represents the most traditional form of FBG: a Type I grating written using the phase mask method with an excimer UV laser. After many years of experience fabricating this kind of grating, the manufacturing process has become highly effective at achieving very high reflectivity, as exemplified in this grating.

FBG 2 is a specialty FBG differing from FBG 1 in that it is chirped. This provides a very wide bandwidth. The chirp rate is quoted as 1 nm in reflected wavelength per 1

mm of grating length. This corresponds to a chirp rate of approximately 0.0034 nm in grating period per 1 μm in grating length.

FBG 3 is an older sample of FemtoFiberTec's point-by-point written FBGs. The manufacturing process for this grating uses high-power infrared femtosecond laser pulses to produce Type II FBGs. The selectivity and control provided by this writing technique allows for intentional apodization to remove sidelobes, as in this FBG. The resulting bandwidth is very low.

FBG 4 is a newer sample from FemtoFiberTec with the same writing technique as FBG 3 but with a few years of process improvement represented. This product is designed for a higher reflectivity than FBG 3 and showcases an even smaller bandwidth. The fiber used for this FBG is SMF-28 Ultra, which differs from standard SMF-28e+ fiber only in that it has tighter specification limits for measures such as attenuation and dispersion [106].

Plots of measured reflectivity spectra around the center wavelength of each FBG provided by the respective manufacturer are shown in Figure 9.

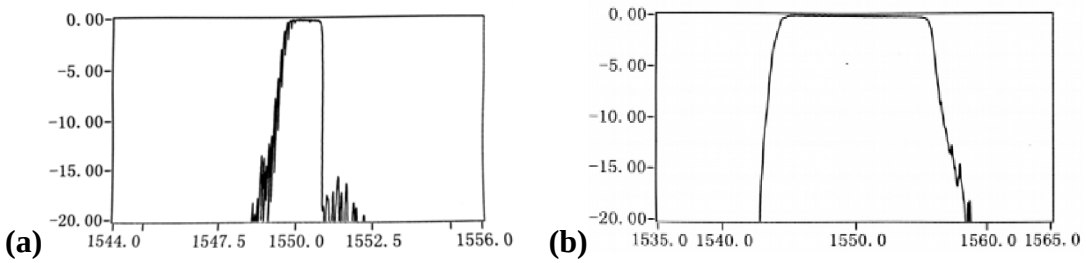

(a) **(b)**

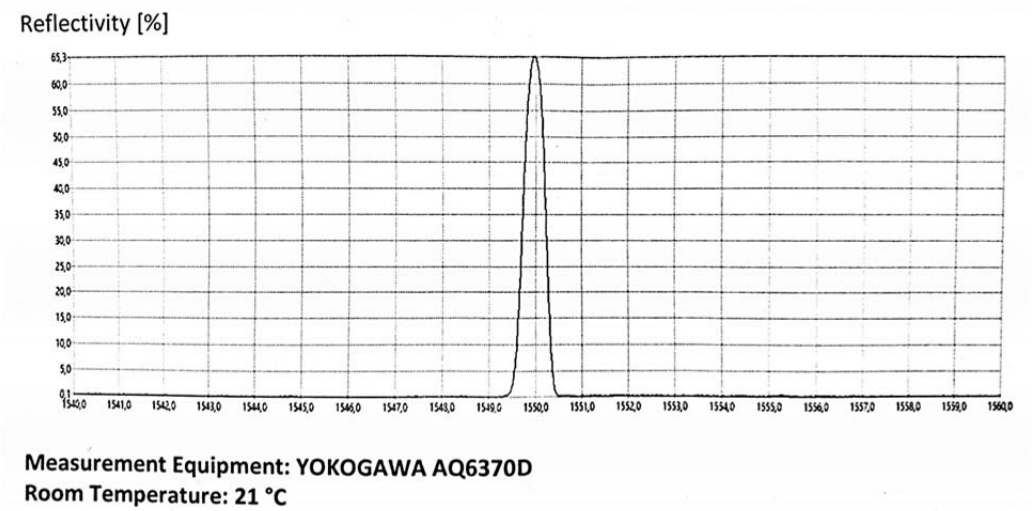

(c)

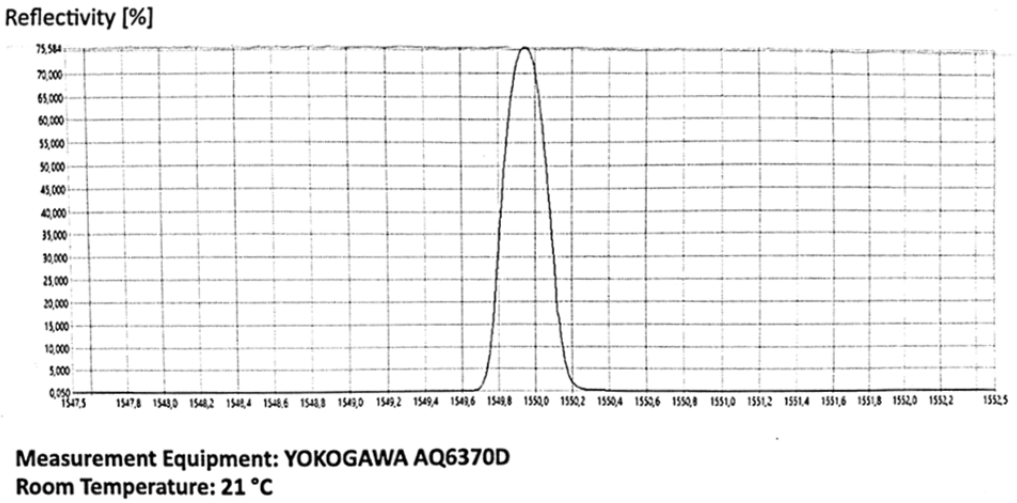

(d)

Figure 9. Reflectivity spectra with horizontal axis in nm of (a) FBG 1 with the vertical axis in dB, (b) FBG 2 with the vertical axis in dB, (c) FBG 3 with the vertical axis in %, and (d) FBG 4 with the vertical axis in %. Larger copies of (c) and (d) are included in Appendix A.

4.4.2 Recovered Core RI Profiles

In this section, the results are analyzed after running the TDPM algorithm as if all through-focal series contain the same data as a single through-focal series; in other words, the same data from images collected at one angle is back-projected from all 15 angles. This procedure is referred to as "single-angle" 3D TDPM as opposed to "full" 3D TDPM that is normally run. Single-angle 3D TDPM implies an assumption of cylindrical symmetry and cannot accurately represent the spatial distribution of components in the sample that lack cylindrical symmetry. However, single-angle 3D TDPM makes it so that no registration along the y-axis is necessary and the grating images are all "in-phase" with each other to represent an accurate RI modulation intensity in the fiber core in the recovered RI distribution. This is why the core RI profiles and their corresponding characteristic functions are determined using this method. Spatial distributions of features and periodicities in the x and z directions are examined later with full 3D TDPM.

The x and z position at which the 1D core RI profile is selected from the single-angle 3D TDPM results differs slightly for each FBG to provide a somewhat representative sample of the modulation amplitude in the core. High-frequency modulation is clearly present in each profile, but to separate noise from the FBG's periodic structure(s), the fast Fourier transform (FFT) algorithm is run to recover the discrete Fourier transform (DFT) of the profile and reveal the strength of different spatial frequencies in the profile. Before running the FFT, the mean RI of the profile is subtracted to remove the DC component, and the profile signal is zero-padded so that the frequency resolution is improved without otherwise altering the output. Since the DFT of

a real signal is symmetric, only half of the output DFT is analyzed. This output is scaled to represent the RI modulation amplitude at the specified spatial frequency.

FBG 1's core profile and spectral content in spatial frequency as described are shown in Figure 10.

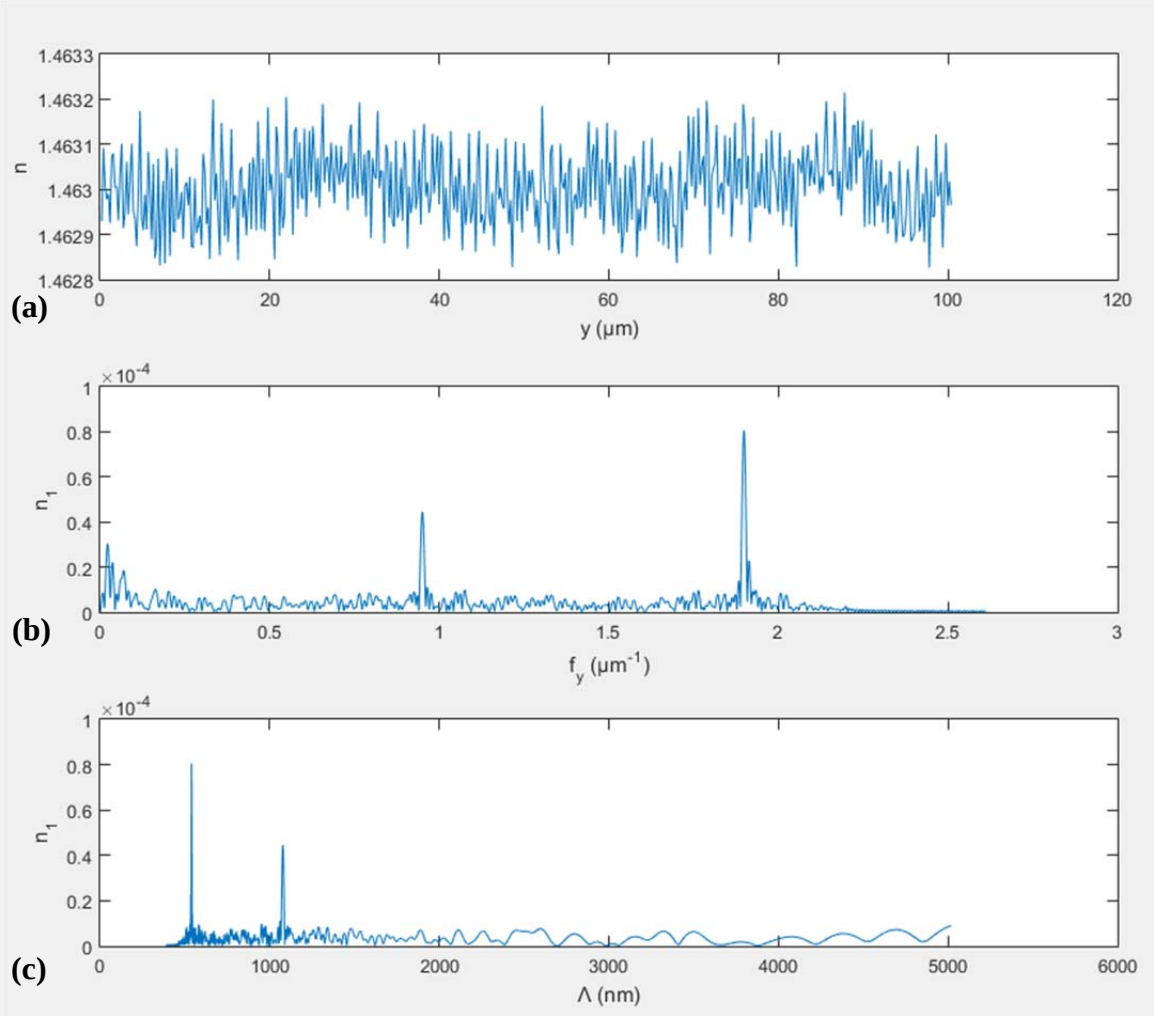

Figure 10. (a) Core RI profile of FBG 1, (b) spatial frequency content of FBG 1, and (c) spatial frequency content of FBG 1 with corresponding period on the horizontal axis.

FBG 1's recovered mean core RI is $n_0 = 1.4630$. As shown in Figure 10(c), the strongest periodic component of FBG 1 is at $\Lambda = 539.5$ nm, where $n_1 = 8.060 \times 10^{-5}$. This strong periodic presence near 535 nm confirms that first-order backward diffraction is used in this grating and shows the resolving power of the system to be sufficient for characterizing such small periods. There is also another strong periodic pattern present in the core at a period of 1077.9 nm, very close to double the period of the main peak and suggesting the additional presence of a grating with second-order backward diffraction of light at 1550 nm. This double periodicity is further addressed later using the full 3D TDPM results.

The core profile and spatial frequency content of FBG 2 are shown in Figure 11.

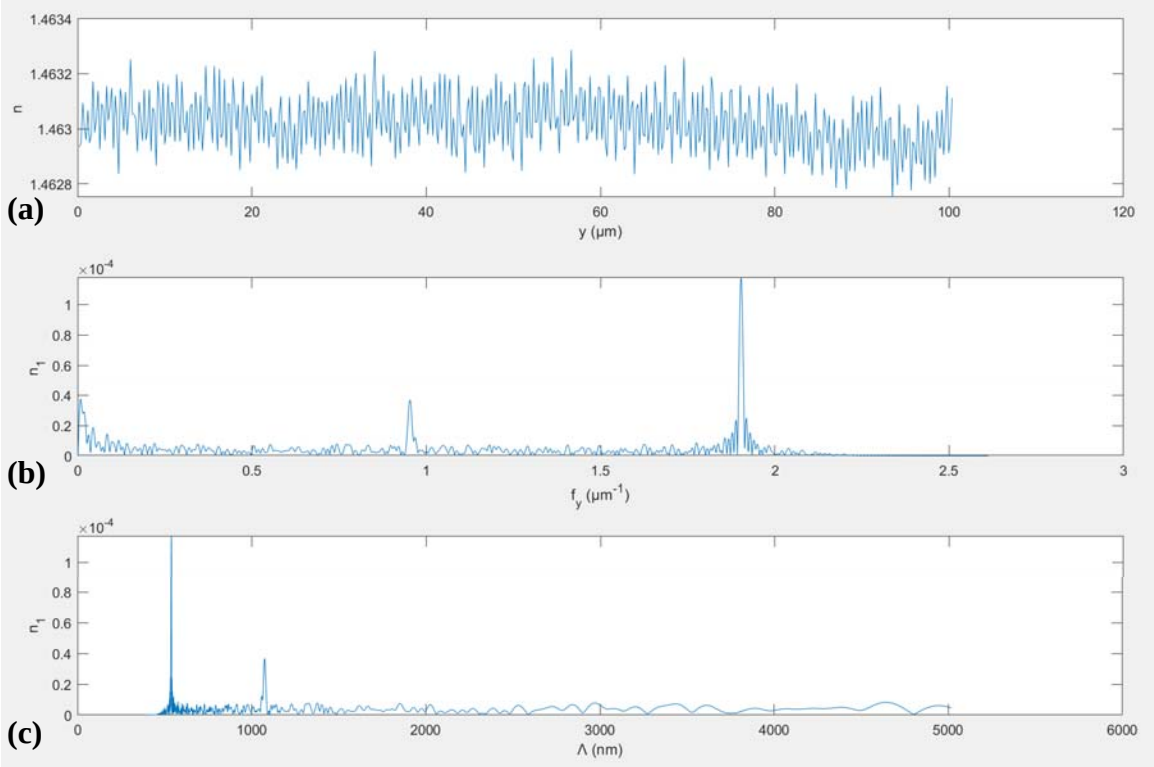

Figure 11. FBG 2's (a) core RI profile and (b-c) spatial frequency content.

FBG 2's recovered mean core RI is also $n_0 = 1.4630$. As shown in Figure 11(c), the strongest periodic component of FBG 2 is at $\Lambda = 538.1$ nm, where $n_1 = 1.1733 \times 10^{-4}$. This means first-order backward diffraction is also used in this grating. There is another peak at close to double the period of the main peak so that some second-order backward diffraction likely also occurs as in FBG 1. Although the chirp is very small across this profile, its effects can be seen in the stronger presence of spatial frequencies surrounding the two main peaks (broader main lobes and higher sidelobes) compared to FBG 1.

The core profile and spatial frequency content of FBG 3 are shown in Figure 12.

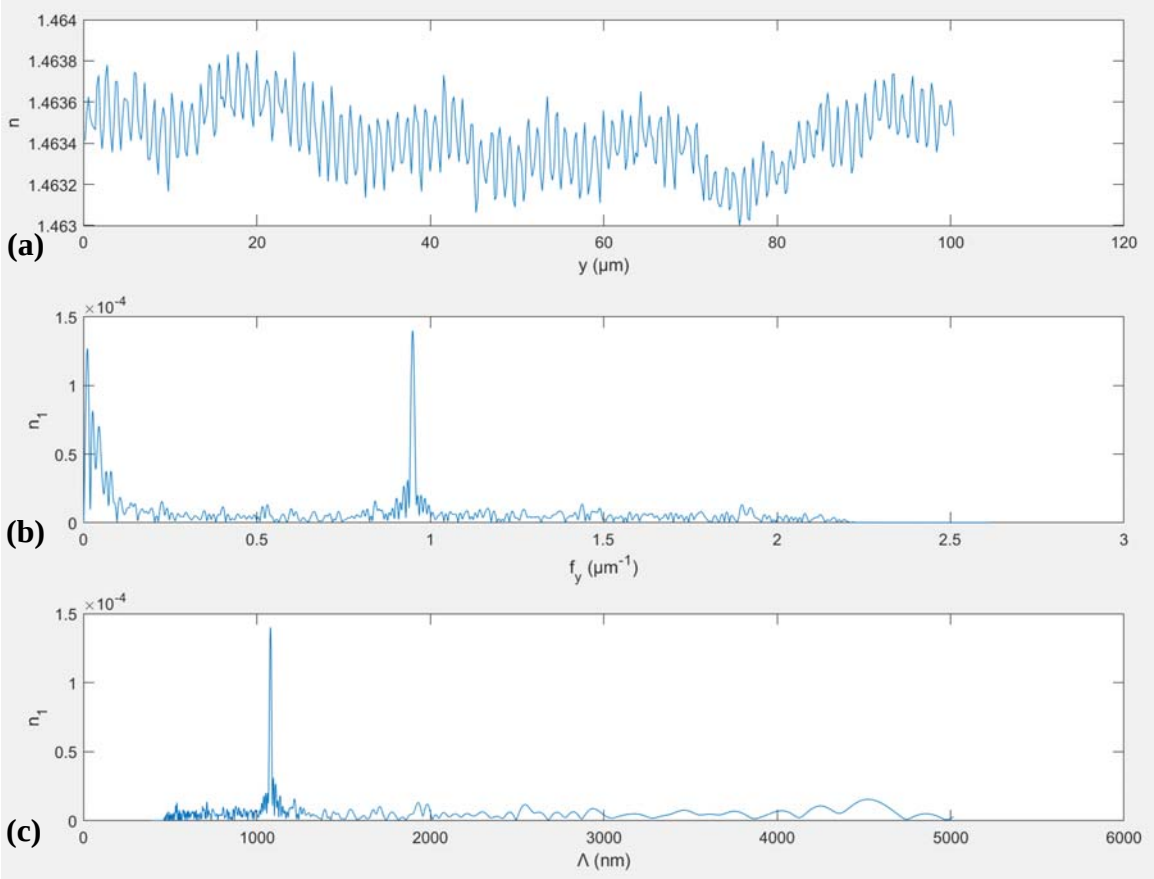

Figure 12. FBG 3's (a) core RI profile and (b-c) spatial frequency content.

FBG 3's recovered mean core RI is $n_0 = 1.4634$. As shown in Figure 12(c), the strongest periodic component of FBG 3 is at $\Lambda = 1079.1$ nm, where $n_1 = 1.4639 \times 10^{-4}$. This strong periodic presence near 1060 nm reveals that this grating is designed for second-order backward diffraction. Relatively high RI modulation amplitude is necessary for the grating length to be so short and still have a reflectivity of 65.3%, and Type II grating fabrication is best suited to producing high RI modulation amplitudes, as exemplified in this grating. A strong low-frequency component is also present, but it is not known whether this is due to noise or due to imperfections in the writing process.

The core profile and spatial frequency content of FBG 4 are shown in Figure 13.

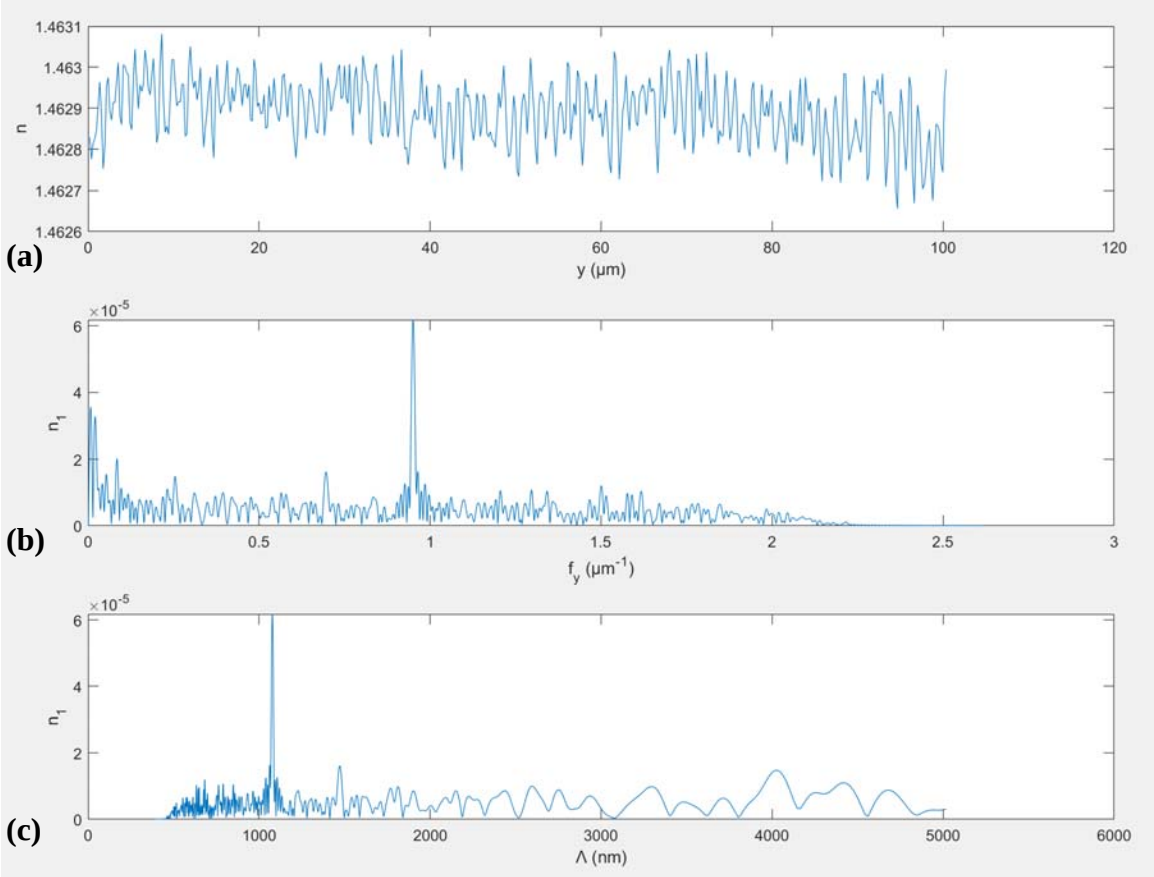

Figure 13. FBG 4's (a) core RI profile and (b-c) spatial frequency content.

FBG 4's recovered mean core RI is $n_0 = 1.4629$. As shown in Figure 12(c), the strongest periodic component of FBG 3 is at $\Lambda = 1077.9$ nm, where $n_1 = 6.176 \times 10^{-5}$. This means this grating is also designed for second-order backward diffraction.

The mean RI of the core for each FBG is predicted to be around 1.4620, the typical core RI of SMF-28 without any FBGs.

The specifications in Table 2 allow for estimation of theoretical RI modulation amplitude of each FBG through the Bragg regime diffraction efficiency approximation. This estimation assumes no nonlinearities such as apodization or chirp, but it still offers an important value for comparison with the recovered RI profiles. The diffraction efficiency, or reflectivity, of a Bragg grating is estimated by:

$$\eta = sin^2\left(\frac{\pi n_1 d}{\lambda \cos\theta'}\right) \quad (9)$$

where η is the diffraction efficiency (i.e. reflectivity), d is the grating length, λ is the center wavelength, and θ' is the angle of incidence from the grating vector direction [14]. Here, θ' is approximately zero due to the guided-mode nature of the incident wave. Thus, the predicted RI modulation amplitude is given by $n_1 = \frac{\sin^{-1}(\sqrt{\eta})\lambda}{\pi d}$.

Equations (1) and (2) allow for calculation of the predicted grating period for the main diffraction order used in each FBG based on the center wavelengths in Table 2. Assuming average RI, RI modulation amplitude, and period to be constant across the recovered profile, their theoretical and recovered values are compared in Table 3.

Table 3. Comparison of theoretical and experimentally recovered average RI, RI modulation amplitude, and period for each grating.

		FBG 1	FBG 2	FBG 3	FBG 4
Main Diffraction Order		1	1	2	2
Average RI n_0	Theoretical	1.4620	1.4620	1.4620	1.4620
	Recovered	1.4630	1.4630	1.4634	1.4629
	Absolute Error	1.0×10^{-3}	1.0×10^{-3}	1.4×10^{-3}	0.9×10^{-3}
RI Modulation Amplitude n_1	Theoretical	7.735×10^{-5}	$>7.702\times10^{-5}$	1.4974×10^{-4}	8.815×10^{-5}
	Recovered	8.060×10^{-5}	1.1733×10^{-4}	1.4639×10^{-4}	6.176×10^{-5}
	% Error	4.20%	<52.34%	-2.24%	-29.94%
Grating Period Λ	Theoretical	535.0 nm	534.9 nm	1069.7 nm	1069.7 nm
	Recovered	539.5 nm	538.1 nm	1079.1 nm	1077.9 nm
	% Error	0.84%	0.61%	0.88%	0.77%

The recovered average RI data for all FBGs is higher than in standard SMF-28 fiber cores by about 1.0×10^{-3}. This could be due to several factors at play. The first is that the writing of the FBG increases the RI in the modulated regions, which brings up the average RI as well, but typically only by about half the RI modulation amplitude. Since the error in average RI is an order of magnitude greater than the RI modulation amplitude, this does not account for much of the error in average RI. The most likely cause for most of the systematic error in average RI is an inaccurate reference RI provided by the surrounding oil medium. Since TDPM only directly recovers relative phase and relative RI, a reference RI is needed to determine the absolute RI. An index-matching oil here was used with nominal RI of 1.460, but with the imaged region heating to significantly higher temperature than room temperature (21^{o} C) prior to imaging, the oil is likely subject to significant expansion resulting in a reduction in refractive index. If the oil refractive index was reduced to around 1.459 before imaging, this would account for the error seen. The likelihood of this error source is given additional merit because the recovered cladding RI is around 1.0×10^{-3} higher than in standard SMF-28 as well.

A systematic error appears to be present in grating period as well. This error may also be at least partially explained with thermal effects. Not only the oil, but to a lesser degree the fiber itself expands due to heating. The center wavelengths were quoted from the spectra as measured at around room temperature. Once heated, the period is expected to increase slightly and the center wavelength should increase correspondingly. This has the minor additional effect of lowering the average RI and RI modulation amplitude slightly from the room-temperature case. An additional source of error here is any tensile strain in the fiber produced by clamping at both rotation stages could increase the period accordingly. However, this effect would be expected to show somewhat random variation in error depending on how the fiber is clamped, and the fairly consistent percent error across FBGs here implies that systematic error such as that due to thermal expansion is likely the main cause. It should be noted that the theoretical grating period for FBG 2 assumes that the exact center of the FBG was imaged, making it less reliable, though imaging the center was attempted to the best ability of the experimenter.

FBG 1 and FBG 3 exhibit very low error in RI modulation amplitude compared to the amplitude predicted by Equation (9). FBG 1 has very low precision in the quoted FBG length, making its calculated theoretical value for RI modulation amplitude somewhat less reliable than that of FBG 3. Of course, apodization introduces error in the RI modulation of each of the FBGs imaged, since this is not accounted for in Equation (9). Still, recovered modulation amplitudes so close to the expected values in these cases lends great credence to TDPM's ability to quantitatively recover RI at high resolution.

FBG 2's theoretical RI modulation amplitude calculation is extremely unreliable due to its chirp. Since the grating is chirped, the effective length of the grating at which

the correct period is present to reflect at the wavelength of interest is less than the length of the entire FBG. Thus, the RI modulation amplitude is expected to be significantly higher than the calculated theoretical value. For FBG 2, if the recovered RI modulation amplitude is to be believed, the effective length is approximately two thirds of the overall FBG length.

FBG 4 exhibits significantly lower RI modulation amplitude than expected. One possible cause of this would be that the imaged portion of the FBG may not be at the center of the FBG and has lower amplitude due to apodization. Additionally, the RI profile recovered from single-angle 3D TDPM throughout the core within the imaged region is non-uniform in this FBG, making it difficult to select a single representative line profile to analyze. The most significant non-uniformity is that very close to the center of the core in the RI distribution recovered from single-angle 3D TDPM, the RI modulation amplitude is very high and there are some lower frequencies present. The (non-representative) center core profile and spatial frequency content of FBG 4 are shown in Figure 14. The main peak is still at 1077.9 nm, but the RI modulation amplitude right at the center of the core jumps above 1.6×10^{-4}. The very center of the core is expected to be somewhat reliably spatially represented by single-angle 3D TDPM, since it is centered across all angles of back-projection. Even so, this RI modulation amplitude is dubious, but it could possibly be explained by interaction between the glass damage from the femtosecond laser while writing and the break in continuity of core material at the center of some fiber cores due to the inside vapor deposition fiber production process [107].

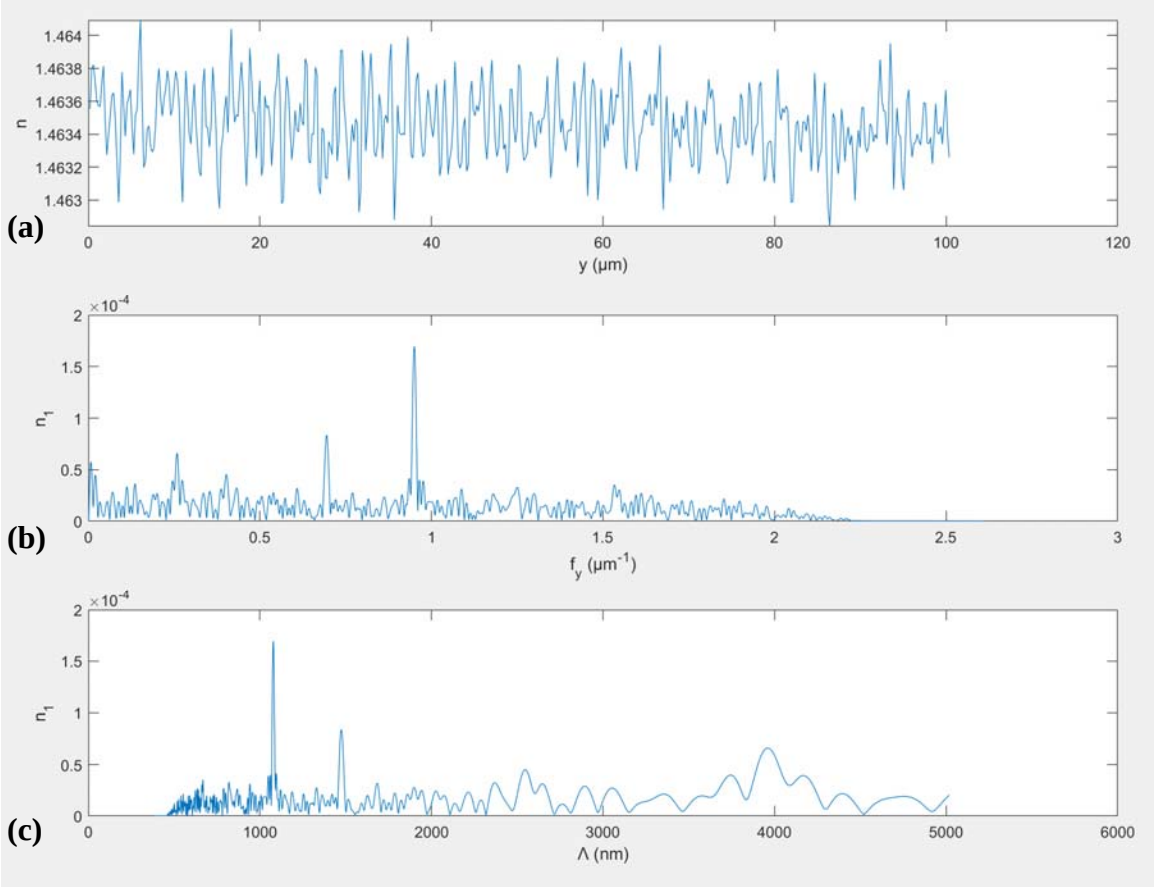

Figure 14. FBG 4's non-representative center (a) core RI profile and (b-c) spatial frequency content.

Additional strong periodic elements are present in the center of the fiber core at periods of 1473.6 nm and 3966.5 nm. Taking a second look at Figure 13 reveals these frequencies may be present to a lesser extent away from the center of the core too, where the original profile was selected. These additional periodicities could possibly be due to current non-idealities of the point-by-point-writing process that keep the waveform from being perfectly sinusoidal. This deviation from simple sinusoidal index modulation may contribute to lowering the reflectivity. A lower reflectivity can sometimes be desired,

however. For example, a network of many weakly reflecting FBGs can provide very high spatial resolution for strain-related sensing applications [108].

4.4.3 Recovered Characteristic Functions

The same core RI profiles obtained in section 4.4.2 are used to recover the characteristic functions with the method outlined in Figure 5(c) and exemplified with with simulation results in Figure 6. These are graphed and compared to the corresponding theoretical constant values for the apodization function (RI modulation amplitude) and the chirp function (grating period) from Table 3 in Figures 15, 16, 17, and 18. The recovered average functions are compared to the average RI of the corresponding profiles to highlight deviation from expected flatness (i.e. constant value).

For FBG 1, as shown in Figure 15, the noise variation in the average function $n_0(y)$ is significant. This casts doubt on the ability to characterize very small defects that affect only the average function, as they must overcome this noise. The apodization function is noisy as well, but with somewhat lower smaller noise magnitude. Applying smoothing or averaging filters would improve the appearance but would remove the ability to characterize defects at a small scale. The chirp function is nearly flat other than at the ends of the imaged region, which are prone to extreme error due to the nature of the applied Savitzky-Golay differentiation filter. However, the rising value of the chirp function followed sharply by rapid decline near the right end of the profile implies a small discrete-phase-shift-like artifact exists in the grating at around $y = 95$ μm.

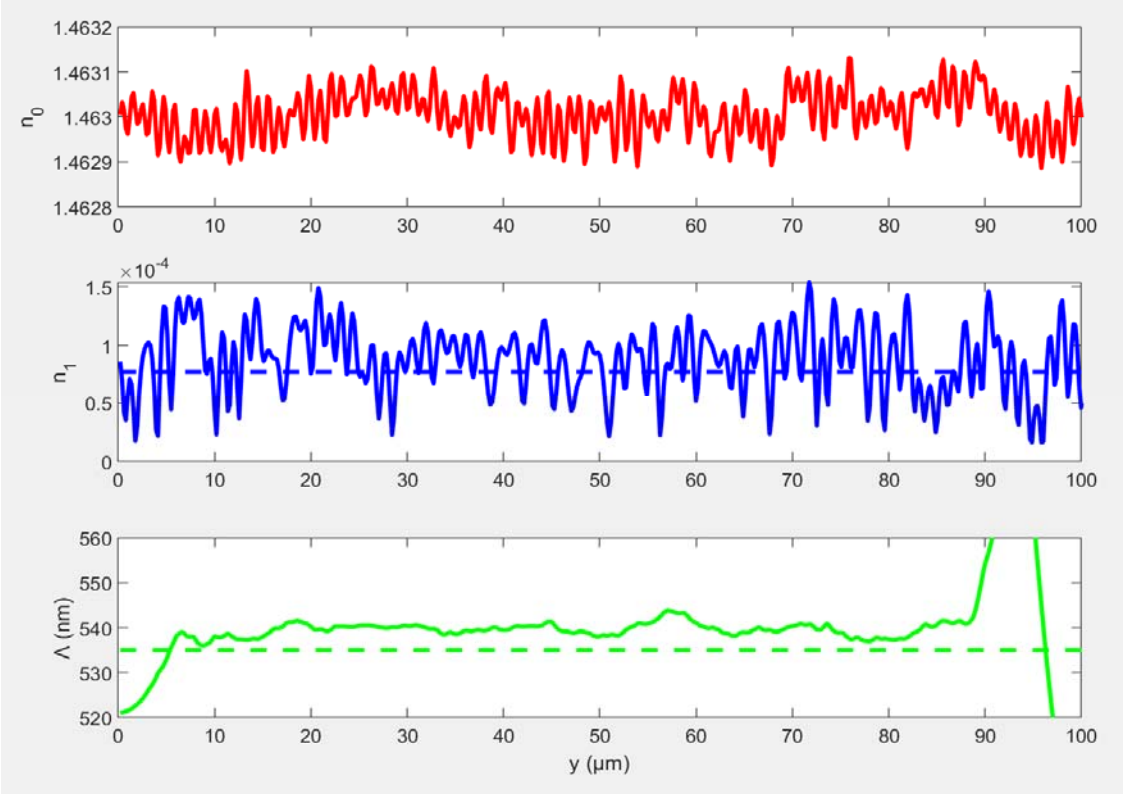

Figure 15. FBG 1's recovered characteristic functions (solid lines) compared to expected characteristic functions (dashed lines).

In FBG 2, the resulting functions are similar in noise to FBG 1, as seen in Figure 16. The theoretical chirp function appears flat, but its graph includes the assumption of linear positive grating chirp rate (i.e. slope) of 0.0034 nm per 1 μm. Theoretically, the period only changes by around 0.34 nm across the recovered profile, which in practice is mostly drowned out by error since the noise-induced variation in the chirp function is an order of magnitude greater than this expected change in period. Applying a linear regression to fit the central 80% of the recovered chirp function (to exclude the end effects) to a linear slope yields a slope of 0.0027 nm per μm, reasonably close to the expected value. However, this linear regression result does not mean much considering the estimated slope varies greatly with the region selected for the regression to fit.

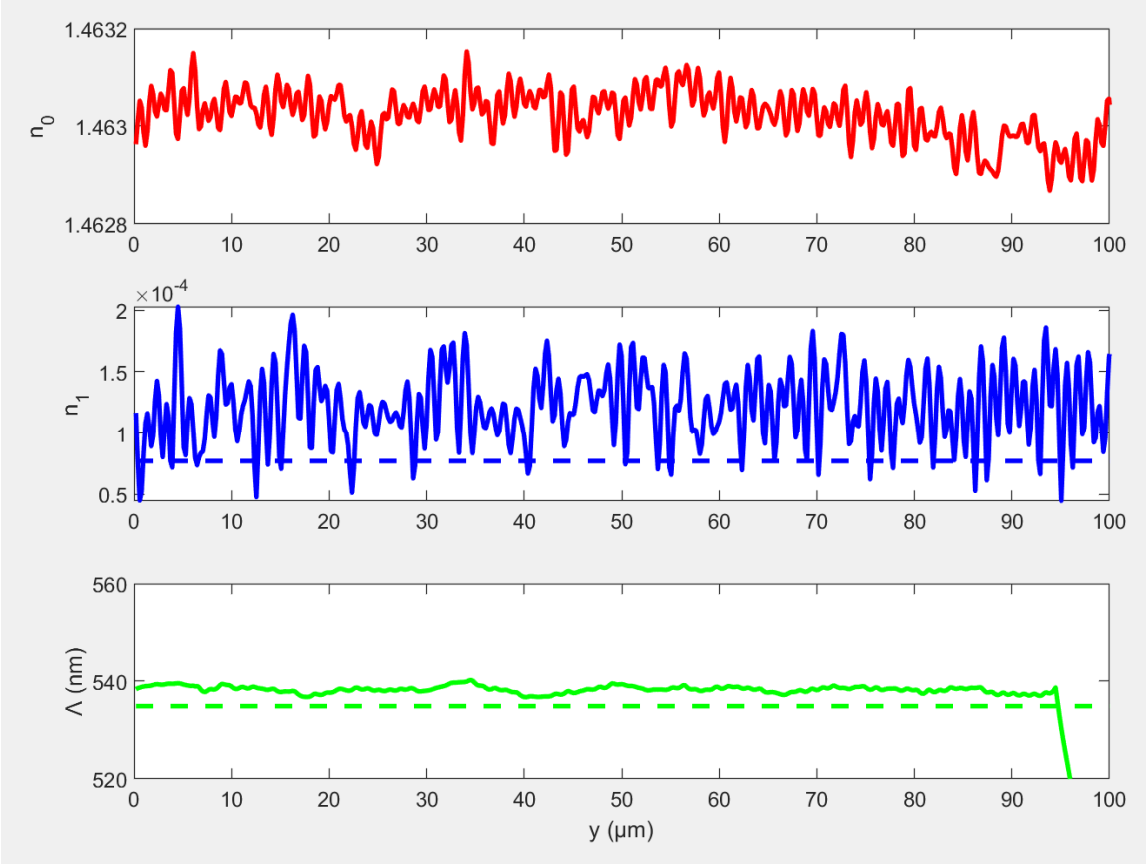

Figure 16. FBG 2's recovered characteristic functions (solid lines) compared to expected characteristic functions (dashed lines).

FBG 3's average function in Figure 17 shows by far the most significant variation of the recovered average functions of the FBGs imaged, in agreement with the significant low-frequency variation observed in Figure 12(a). The reason for this strong low-frequency content is not known but could possibly be explained by the writing process lacking refinement at the time of production, as the newer FBG 4 made using the same technique does not exhibit this level of variation, as seen in Figure 18. Additionally, FBG 3's chirp function varies from flatness more than that of FBG 1. The apodization function exhibits similar relative noise variation to other FBGs imaged.

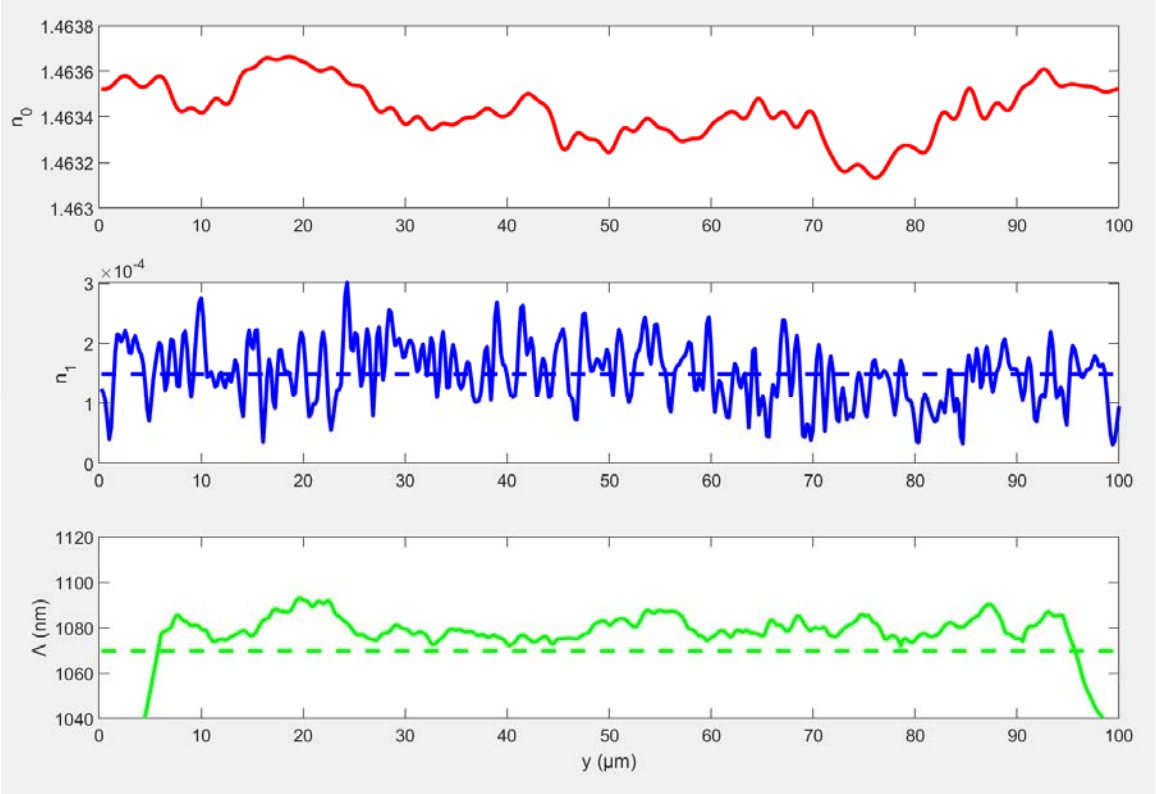

Figure 17. FBG 3's recovered characteristic functions (solid lines) compared to expected characteristic functions (dashed lines).

Noise in the average and apodization functions of FBG 4 (shown in Figure 18) is similar to that seen in the other imaged FBGs. The chirp function here varies to a much greater extent than in the other FBGs imaged. This is not straightforwardly explained by the presence of the longer-period components in FBG 4 since lower than expected periods are shown in the recovered chirp function, but the two observations may be related. Greater variation in period appears to be present in both point-by-point-written FBGs compared to those written with the phase mask technique. This could potentially be explained by positional error in the laser as it translates along the fiber to write the FBG. However, this is counter to the narrower reflection bandwidth exhibited by these FBGs, which would seem to imply less variation in period, so these effects may be local.

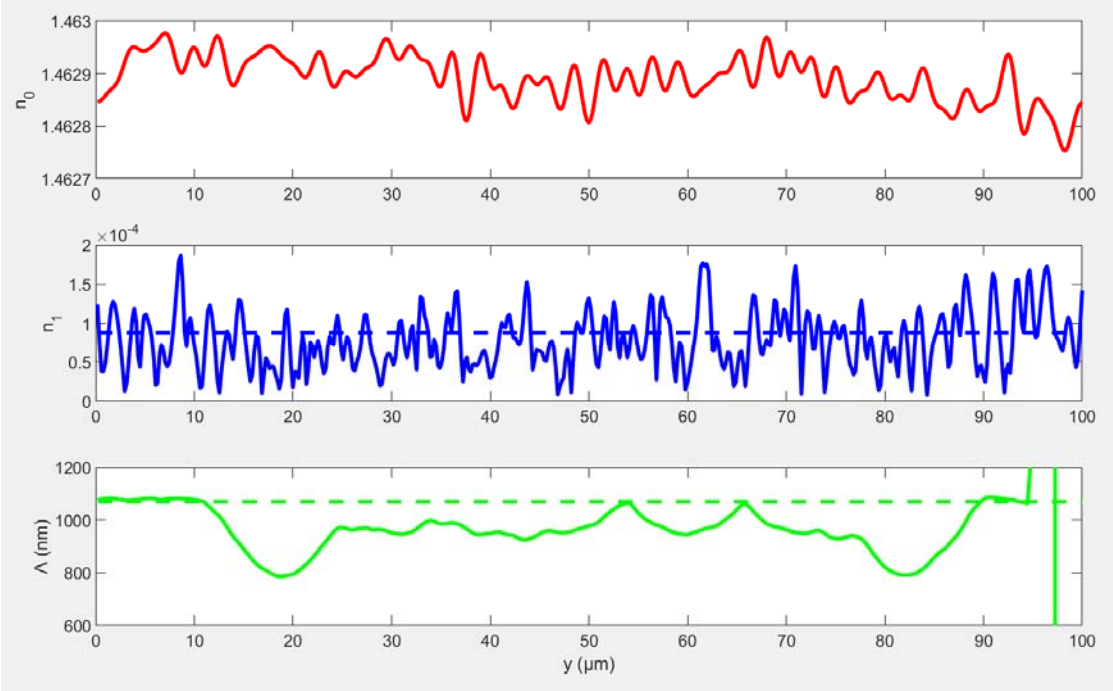

Figure 18. FBG 4's recovered characteristic functions (solid lines) compared to expected characteristic functions (dashed lines).

4.4.4 Recovered 3D RI Distributions

Full 3D TDPM, with all angular data back-projected as intended, results in a spatially accurate RI distribution in the x and z directions, though it is not entirely accurate in the y-direction due to lack of registration along the fiber axis. However, the presence of frequencies in the y-direction in the resulting 3D RI distribution should be accurate other than having a reduced amplitude.

To demonstrate simple RI recovery from full 3D TDPM, a section of SMF-28 with no grating was imaged, and the resulting 3D RI distribution is shown in Figure 19. The recovered core RI in this sample is comparable to the average core RI seen in the FBGs, supporting the assertion that the oil RI is slightly less than 1.460 during imaging.

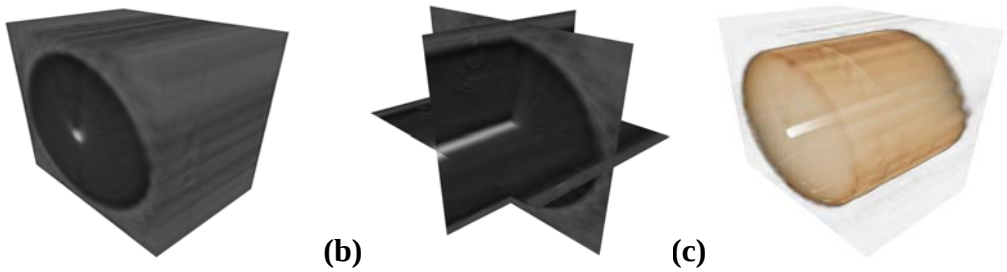

Figure 19. Recovered 3D RI distribution of SMF-28 shown as (a) an opaque block with higher RI shown with greater brightness, (b) three 2D center cross sections of the same opaque block, and (c) a visualization in the style of a typical 3D magnetic resonance imaging (MRI) image with opacity varying with RI.

The core and cladding are clearly visible in all three images in Figure 19. The following FBG analysis primarily uses 2D center cross sections of the recovered 3D RI distributions, such as those displayed in Figure 19(b).

The center xy cross section of FBG 1's RI distribution resulting from full 3D TDPM is shown in Figure 20(a), with brighter pixels signifying higher RI, as denoted by the bar on the right side. The periodic grating pattern(s), though not as strong as they should be due to lack of y-direction registration, can still be faintly seen. However, just as the spectral content of FBG 1 is more clearly analyzed in Figure 10(b) than in Figure 10(a), Figure 20(b) uses a similar 1D FFT procedure line-by-line to display the y-direction spatial frequency content of each profile in the center xy cross section, with brighter pixels signifying higher RI modulation amplitude, though the scale shown in the bar on the right side is reduced from the actual RI modulation amplitude (again, due to lack of y-direction registration). Horizontal white lines are drawn over this image to represent the core and cladding boundaries – these lines do not signify the presence of all or any spatial frequencies at these locations.

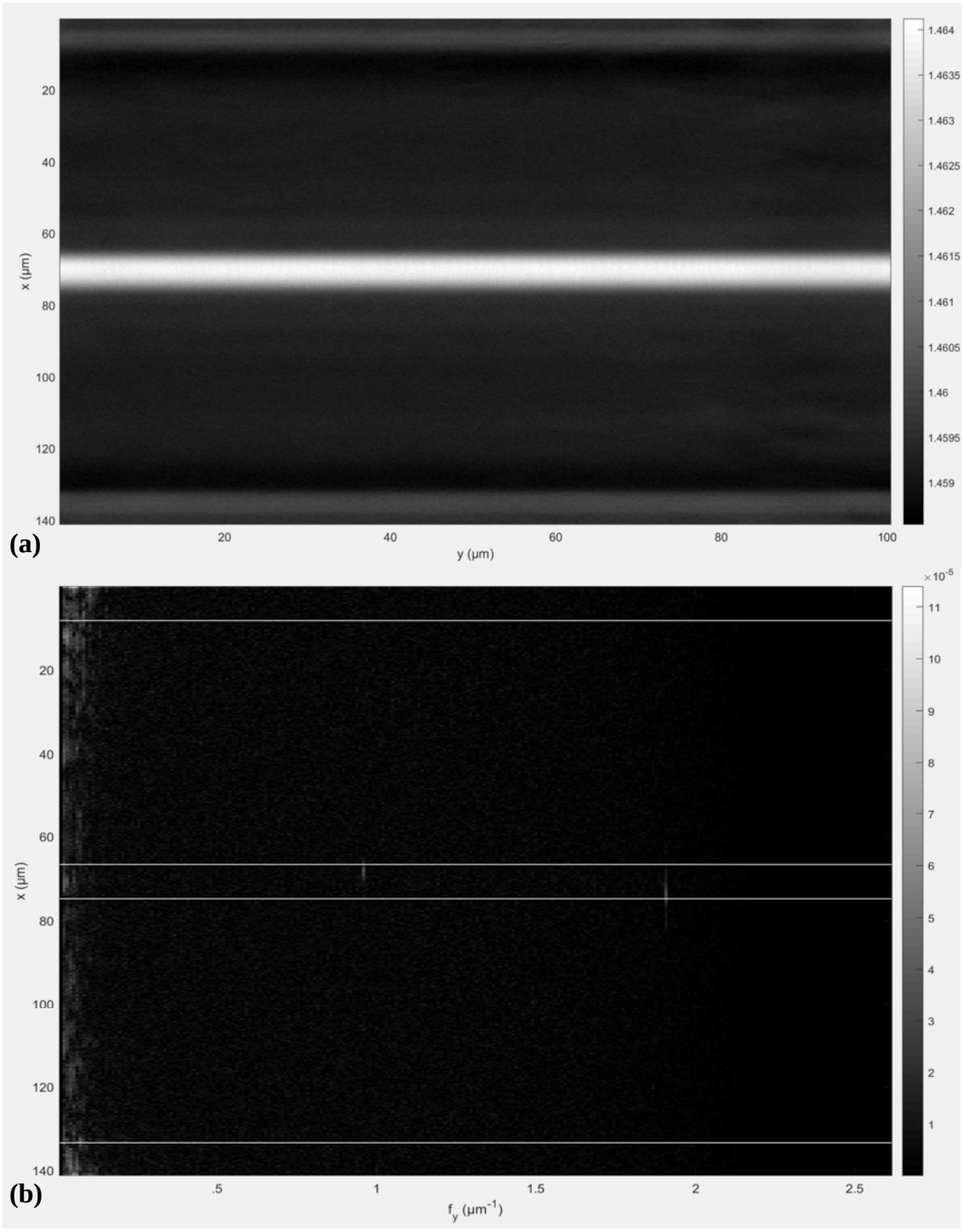

Figure 20. (a) Center xy cross section of RI profile of FBG 1 and (b) y-direction spatial frequency content of FBG 1 with core and cladding boundaries marked.

This clearly shows that the 1077.9 nm periodicity is present on one side of the core and the 539.5 nm periodicity is present on the other. As imaged, the x-direction was aligned with this variation allowing for this disparity in period to be seen without rotating from the default coordinate system. Closer visual inspection of Figure 20(a) reveals a longer period along the upper side of the fiber core and shorter period along the lower portion of the core, though difficult to see with low RI modulation amplitude.

The presence of these two separate periods in the fiber core can possibly be explained by the Talbot effect [109]. When a simple phase mask is used to write a grating, the interference pattern is not constant (and is in fact periodic) with respect to distance from the phase mask in the near field. If the dual-period pattern seen in this fiber is to be interpreted as a result of the Talbot effect, then the phase mask was placed approximately on either the $+x$ or $-x$ side of the fiber during writing. The phase mask periodicity was in the y-direction. Since the largest period present in a Talbot pattern is the period of the phase mask, the phase mask period is assumed to be 1077.9 nm. At a quarter of the Talbot length (the distance in the x-direction at which the interference pattern repeats itself), the interference period in the y-direction is one half the phase mask period [109], corresponding to the 539.5 nm period seen in this fiber. Since the transition between these two periodic regions in the fiber appears to occur approximately across the core diameter, it is assumed that the core diameter is approximately one quarter of the Talbot length, meaning the Talbot length is approximately 32 μm.

The Talbot length in free space can be calculated as:

$$x_T = \frac{\lambda}{1-\sqrt{1-\frac{\lambda^2}{\Lambda_{pm}^2}}} \quad (10)$$

where Λ_{pm} is the phase mask period [110]. This calculation also works consistently if all values are the values inside a medium of nearly constant RI. Given the assumed phase mask period and Talbot length, the predicted wavelength of the laser light used to write the FBG and generate the supposed Talbot pattern can then be calculated as approximately 72.5 nm in the fiber core. Multiplying the wavelength in the core by the RI of about 1.462 yields a free-space wavelength of 106 nm. This casts some doubt on the accuracy of the assumptions made about this pattern, as FBGs are rarely written with lasers with a wavelength below 157 nm [111]. However, since a large amount of error may be introduced by attempting to estimate the Talbot length from only a small portion of a Talbot pattern recorded in the fiber core, it is possible that any discrepancy is due largely to errors in estimated quantities.

In any case, the ability of TDPM to spatially characterize distinct periodicities in 3D with high resolution in all directions is demonstrated here and shows promise in revealing artifacts and patterns that have yet to be observed in FBGs.

The center xy cross section of FBG 2's RI distribution resulting from full 3D TDPM and the corresponding line-by-line spatial frequency content in the y-direction are shown in Figure 21.

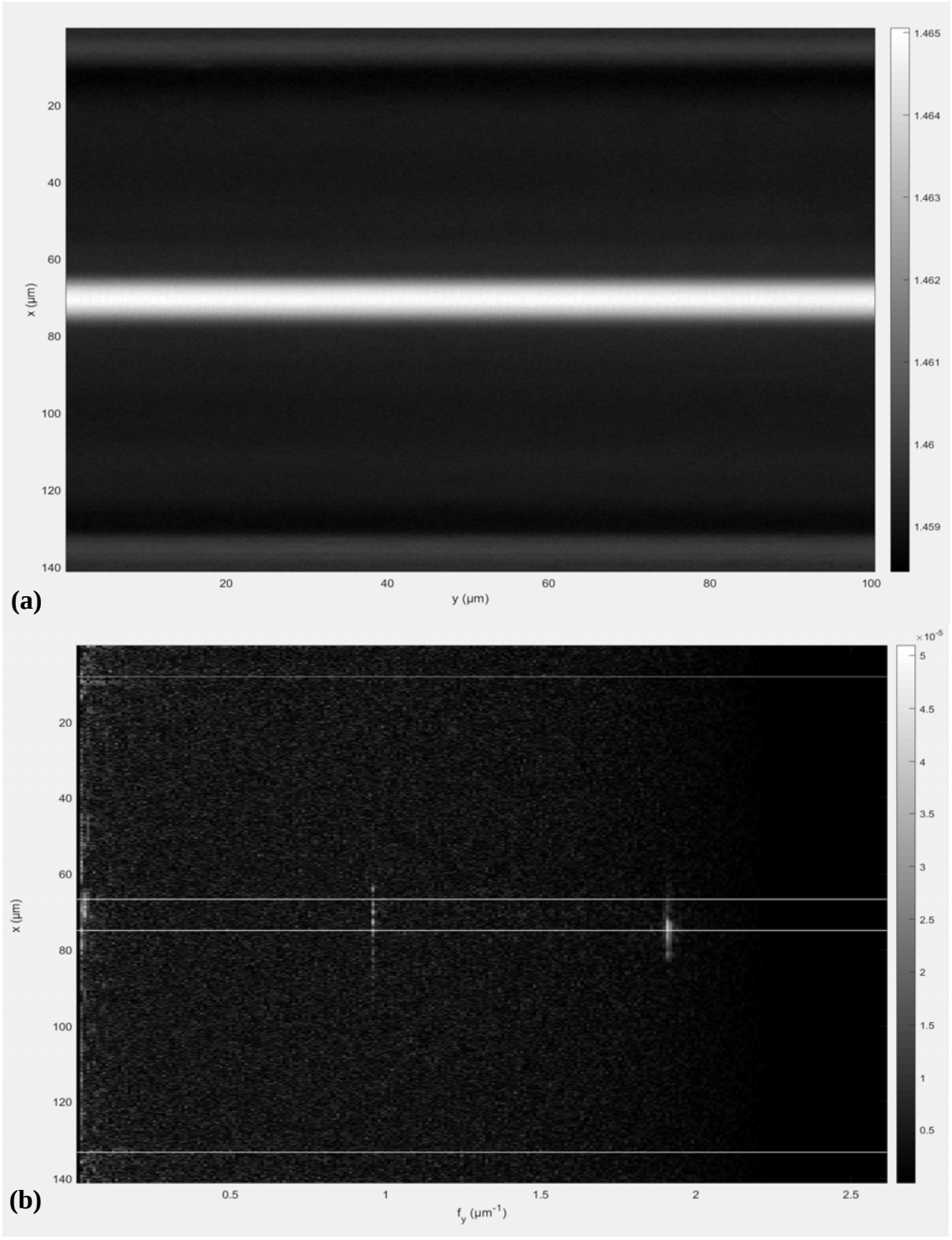

Figure 21. (a) Center xy cross section of RI profile of FBG 2 and (b) y-direction spatial frequency content of FBG 2 with core and cladding boundaries marked.

If the presence of chirp was not readily apparent by comparison of the spectral widths of spatial frequency content of FBG 2 and FBG 1 in Figure 11(b) and Figure 10(b), respectively, the difference is unmistakable when comparing Figure 21(b) and Figure 20(b). Figure 21(b) shows a wider presence of spatial frequencies around the main spatial frequency in FBG 2, while Figure 20(b) shows an extremely narrow frequency presence in FBG 1 – only one pixel at the spatial frequency resolution shown. This clear ability to distinguish the presence of chirp, even though chirp rate is not yet reliably able to be recovered, bodes well for the future applications of TDPM in FBG characterization.

The spatial frequency content varies across the core of FBG2 as it does in FBG 1, but with a more complicated pattern. The cladding also contains significant RI modulation, possibly due to the longer exposure required to generate the higher core RI modulation amplitude exhibited by FBG 2. The presence of a longer period (lower spatial frequency) varies rapidly in the x-direction, apparently periodically, unlike the main periodicity around 538.1 nm. The exact reason for this is unknown, but it could potentially be explained through a complicated interference pattern similar to a Talbot pattern but accounting for a chirped grating.

The center xy cross section of FBG 3's RI distribution resulting from full 3D TDPM and the corresponding line-by-line spatial frequency content in the y-direction are shown in Figure 22. The RI distribution for FBG 3 appears somewhat blurrier than in FBG 1 and FBG 2. It is believed this is due to an experimental failure to adjust the system to ensure proper Köhler illumination prior to imaging. Additionally, some small artifacts were stuck to the cladding that can be seen in the lower left of Figure 22(a).

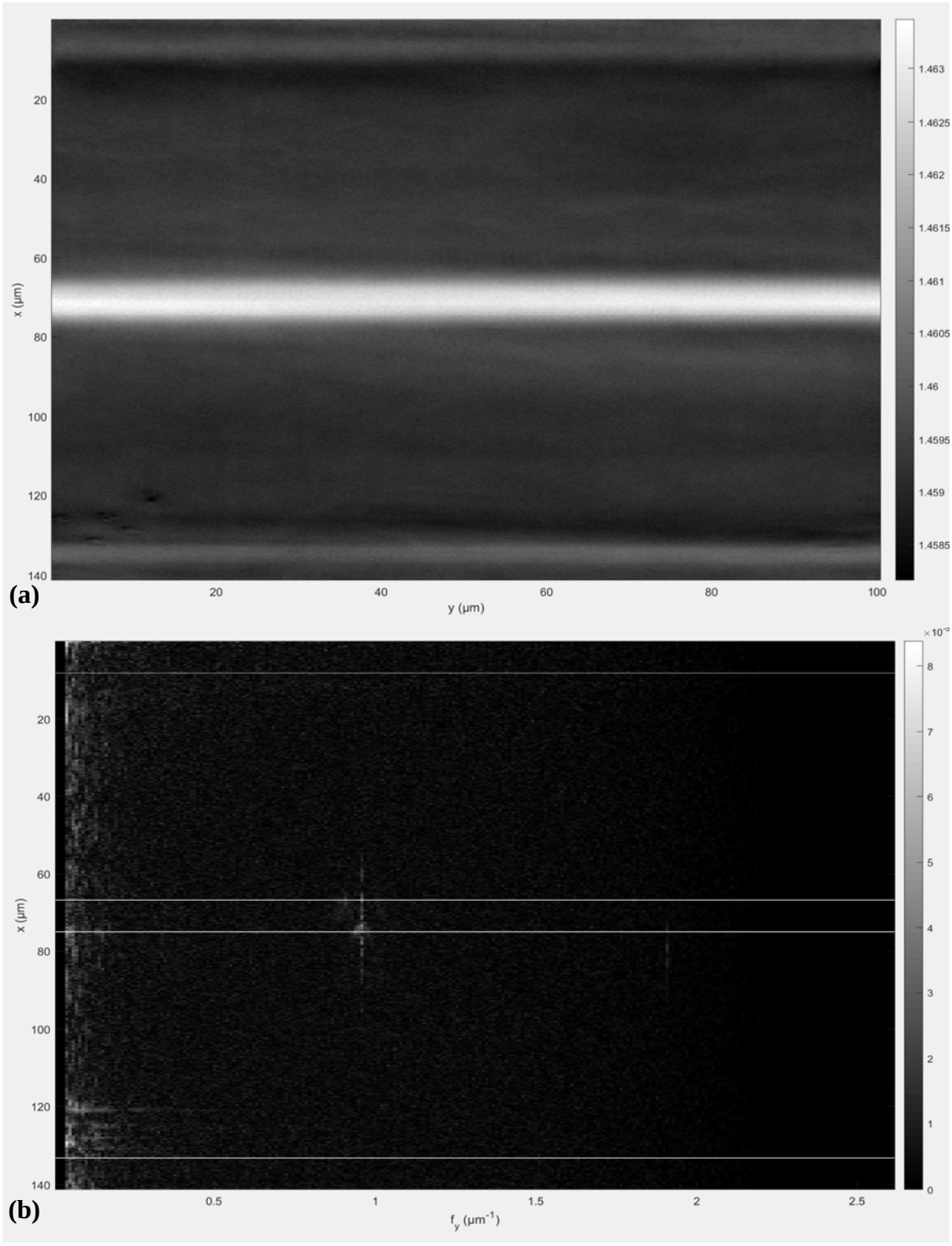

Figure 22. (a) Center xy cross section of RI profile of FBG 3 and (b) y-direction spatial frequency content of FBG 2 with core and cladding boundaries marked.

FBG 3's RI modulation amplitude appears to be strongest at the lower side of the core in Figure 22(b). This could mean the laser was directed at the $+x$ side of the fiber during the writing process, inducing greater modulation on that side. The RI modulation amplitude generally decays away from this x-position, extending into the cladding on both sides. As this FBG is written by a high-power laser to induce a high core RI modulation amplitude, it follows that the cladding here exhibits some degree of modulation as well. At the lower core-cladding boundary, where RI modulation amplitude is highest, there is a faint presence of spatial frequencies around the center spatial frequency. Greater damage to the glass structure here, where the laser was likely focused at the highest intensity, may make the resulting RI distribution and its period slightly unpredictable. Additionally, FBG 3's RI modulation amplitude exhibits a semi-periodic pattern in the x-direction, somewhat like that seen at the lower spatial frequency in FBG 2 in Figure 21(b). The reason for this is unclear.

FBG 3 also exhibits very slight RI modulation at near double the spatial frequency of its main periodic component, present only in the cladding near the lower side of the core in Figure 22(b). This may possibly be explained as slight presence of a non-ideal harmonic frequency that did not form in the core, where the fabricated RI distribution is important for reflectivity and is more nearly sinusoidal.

Full 3D TDPM was not able to be completed for FBG 4, as the data from one or more angles was corrupted.

CHAPTER 5

RESEARCH SUMMARY AND FUTURE WORK

5.1 Summary of Completed Work

The immediate objective of this research was to extend and apply tomographic deconvolution phase microscopy to achieve highly effective quantitative phase imaging of fiber Bragg gratings. This was completed by 1) preparing a physical configuration to overcome challenges of FBG imaging, 2) tweaking image processing techniques to produce the best results from FBG images, and 3) imaging and analyzing various types of FBGs to demonstrate the capabilities of this technique.

A dual rotation stage and a higher numerical aperture of the condenser lens were implemented for this research. The camera's pixel sensors were analyzed and confirmed to be sufficient for this research.

Regarding image processing, generation time for accurate PSFs was greatly decreased, a cleaner result was obtained by cropping the PSF, and registration success rate was improved. To circumvent present experimental difficulties in recovering accurate RI modulation amplitude, image data taken from a single angle was back-projected from all rotation angles for this purpose so that no registration along the fiber axis was necessary. Using only the high-frequency portion of the TDPM algorithm to process all frequencies was found to produce clearer and cleaner images in most cases as well for fiber imaging.

The following types of FBGs were imaged and their characteristic functions recovered:

- Type I First-Order FBG written with Phase Mask
- Chirped Type I First-Order FBG written with Phase Mask
- Type II Second-Order FBG written Point-by-Point

The following capabilities of TDPM were demonstrated:

- High-resolution 3D RI distribution recovery
- Characterization of period, amplitude, and location of RI modulation
- Identification of presence of chirp
- Identification of potential physical effects of manufacturing processes in FBGs

5.2 Future Work in Improving TDPM Methodologies for FBG Imaging

5.2.1 Standard Samples for Analysis of TDPM Accuracy

Though qualitative and quantitative results from the current TDPM methods largely agree with expectations, the accuracy of the recovered RI has not been confirmed against a precisely known standard. A standard sample should be developed to examine the accuracy with which TDPM can recover phase. If phase can be accurately recovered, the RI is simple to recover through calculation and back-projection, which may be analyzed in simulation. This means an effectively 2D sample with varying phase delay through it is sufficient for most analyses. This 2D phase delay pattern may be

accomplished through either varying thickness or varying refractive index. The same effective diffraction pattern can be accomplished through either method. The sample should contain a variety of spatial frequencies with precisely known modulation of thickness or RI. Such a sample could reveal how accuracy of recovered phase depends on spatial frequency and on the position of features in the image, as aberrations may reduce accuracy away from the image center.

Since surface relief variations are easier to fabricate with greater precision and also easier to measure with greater precision than RI variations, an arrayed surface relief pattern is proposed. Electron beam lithography and etching may be used to fabricate such an array with sub-micron feature sizes [112]. In this technique, areas of a flat substrate not selected to be part of the sample pattern can be etched away so that the sample pattern is left on the substrate in the form of ridges. The ridge height can then be very precisely measured via AFM, a technique mentioned in Chapter 2 which is able to achieve sub-nanometer resolution. With a known ridge height Δh, the phase difference between the regions with and without ridges is given by:

$$\Delta\varphi = \Delta h \cdot \frac{2\pi\Delta n}{\lambda} \qquad (11)$$

Where Δn is the difference in RI between the substrate and the surrounding medium, whether it be air, water, or oil.

The Georgia Tech Optics Lab has previously developed such an arrayed test pattern (shown in Figure 23) that would serve these purposes well. It is inspired by the 1951 USAF resolution test chart [113]. To ensure accurate fabrication with available

techniques, the minimum feature size can be 0.5 μm such that the minimum center-to-center ridge spacing is 1 μm. The largest center-to-center ridge spacing in the pattern would then be 6.275 μm. Ideally, minimum feature sizes would be even smaller to examine the accurate recovery of spatial frequencies even higher than those seen in FBGs.

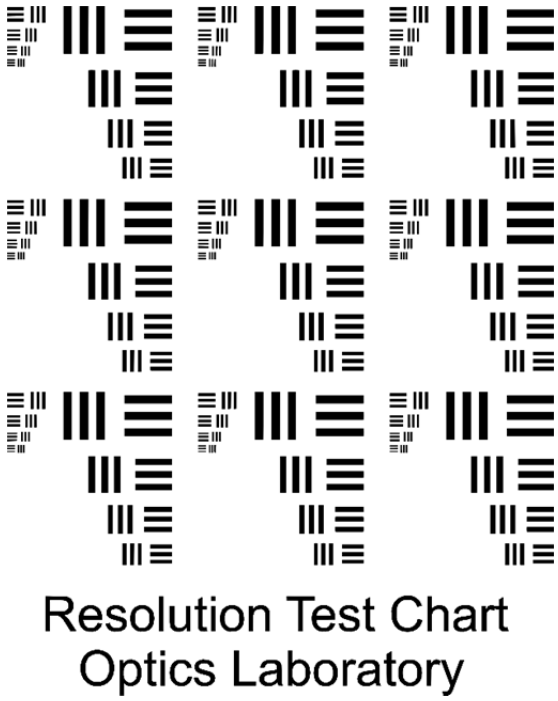

Figure 23. Georgia Tech Optics Lab Resolution Test Chart pattern.

In addition, an ideal sample would be 3D and easily rotated so that the inaccuracies of the back-projection portion of the tomographic processing can be analyzed too. This would reveal effects on recovered RI accuracy and precision due to multi-angle noise reduction as well as registration quality. Acquiring such a 3D sample poses additional significant challenges in representing a range of spatial frequencies at once, fabricating the sample, and precisely measuring the sample after fabrication. The

ideal 3D sample would be a multi-core fiber with highly chirped FBGs, but it is difficult to accurately know the RI of such a sample after fabrication (hence the need for this research). The simulated sample shown in Figure 6 fits this description of an ideal sample very well but is not realistic to create as a known physical object.

5.2.2 Illumination Profiles

A significant potential improvement to TDPM for FBG characterization is the use of annular illumination. Annular illumination is predicted to pass fewer low-frequency components, which are mainly troublesome noise when imaging simple FBGs, and isolate the high frequency components of FBGs for clearer imaging. Bao [114] has completed theoretical analysis of this improvement, and experimental confirmation is the clear next step.

Experimental confirmation should first take place with the proposed 2D sample arrayed surface relief pattern described in section 5.2.1. This would allow testing across a range of spatial frequencies simultaneously. The Gaussian illumination currently in use can be used as a control to compare the results to. The experiment may then be repeated with first-order and second-order FBGs, at which point, if results show improvement, annular illumination may be selected as the best illumination for FBG imaging.

Various annular diameters should be used as are presently available in the form of annular condenser stages designed for phase contrast microscopy. The recovered phase contrast (difference in phase between the ridges and etched region) can then be quantified for both annular and Gaussian illumination for each different spatial frequency and

compared to the theoretical phase contrast given by Equation (11). This value is expected to vary for objects of different spatial frequencies depending on the illumination profile.

5.2.3 System Hardware Components

An obvious improvement to the system would come through a better camera to capture the images. Lower noise from the camera would be highly desired to obtain cleaner resulting images. Also, smaller pixel spacing would correspond to a higher sampling rate, which allows for higher frequency measurement without aliasing and clearer images of gratings up to the diffraction limit. Having higher frequency measurement capabilities allows for better analysis of what harmonics are present in FBG grating "waveforms" since they may not be perfectly sinusoidal in some cases. This may be helpful in differentiating the results of various manufacturing techniques.

The benefits of higher-resolution imaging must be balanced with the downsides in increased data transfer time, data storage capacity needs, and data processing time. With 11,696 images taking up over 29 GB for an entire data set with the current camera and configuration, the storage needs are already significant. Data processing times can take several hours as is, and any increase in number of pixels in one direction will yield an even greater increase in processing time based on the $O(n^3)$ nature of the 3D TDPM algorithm (note that n here does not refer to refractive index but rather the algorithm input size along one dimension of an image). Lower processing time is crucial if TDPM is to be used at industrial scale. Of course, a subsection of the overall image data may be

isolated for use to lower processing time. Efforts may be made to improve the algorithm runtime in the future.

To improve the diffraction-limited resolution of the system, an objective lens designed for oil immersion could allow for a significantly higher numerical aperture. The numerical aperture of an objective lens is defined as $\mathrm{NA_o} = n \sin \theta_\mathrm{o}$, where θ_o is the maximum half-angle of light rays that can still enter the objective lens to be collimated. If the lens is in air with an RI very near unity, the maximum possible practical $\mathrm{NA_o}$ is slightly less than one. Thus, immersing the lens in a higher-index oil could bring the numerical aperture above one and allow for significantly higher spatial frequencies to be imaged, assuming the camera resolution is improved as well.

The piezo scanner currently limits the system in two crucial ways: data collection speed and maximum object thickness. Most of the time spent collecting data is to allow the piezo scanner to move and stabilize the objective lens before capturing each image. The actual image capture time is much shorter in comparison. Most piezo steppers have comparable speed, however. The scan range is another factor that limits the kind of objects that can be imaged. The through-focal series should encompass a range greater than the thickness of the object to capture sufficient data from defocused images for reconstruction. Commercial piezo objective scanners are readily available [115] to provide an expanded range to allow for thicker objects to be imaged, such as bundled, fused, or wrapped multi-fiber FBG sensors in addition to capillaries containing biological samples.

5.2.4 Iterative TDPM

Though TDPM with the current system does not presently require as many rotation angles as other diffraction tomography QPI techniques [77], the time to collect and process the data for each angle is significant. The fiber may need to be adjusted and re-centered after each rotation, taking up more than just the simple image collection time that is required for each angle. Additionally, the majority of the processing algorithms have a runtime directly proportional to the number of rotation angles used. The 15 angles used this experiment are necessary to ensure the "missing cone" problem (POTF values of zero for a conic region in the 3D spatial frequency domain when data is collected at a single angle) is overcome such that all 3D spatial frequencies are represented for the high frequency algorithm to recover.

An iterative constrained operation can be applied to reduce the number of required rotation angles, as developed, simulated, and confirmed (by imaging various fiber types without FBG) by Bao [116]. This is referred to as iterative TDPM (ITDPM) and reduced the required rotation angles to 3 rather than 15 with the current system [116]. It is theoretically possible to have sufficient fiber and FBG characterization through the collection of images at only a single angle, if the missing cone is reduced in size such that no frequencies of interest occur within the missing cone. The missing cone size is reduced by increasing the numerical aperture of the condenser lens, but this also consequently increases the size of low-value region of the POTF, which is problematic because a lower POTF value results in a higher margin of error once inverted. A Gaussian illumination profile can compensate for this by reducing the relative size of the

low-value POTF region (compared to disk illumination) and is thus ideal to use for a single-angle ITDPM approach. Additionally, the assumption of weak absorption proportional to the refractive index contrast may reduce the effects of any zero-value POTF along the y-axis by substituting an effective POTF including these weak absorption effects [117]. Each of these possibilities may be explored and experimentally tested to optimize single-angle ITDPM to a level of practical usability.

5.2.5 Registration

A lingering issue with 3D (non-iterative) TDPM without a clear best solution is registration along the fiber axis, or more generally the axis of rotation. If a periodic structure can be guaranteed to shift less than half a period between angular measurements, a best-fit or highest-correlation algorithm can be applied for registration in this direction. Even with the dual rotation stages introduced in this research, this margin of allowed shifting is not able to be consistently maintained, so this technique cannot be relied on unless a more precise and stable fiber positioning stage is developed. However, for more general cases where objects are not simple periodic structures (e.g. splices, defects, or damages in fibers; cells in biological imaging applications), a more adaptive algorithm is required. The simplest algorithms to do something like this are autocorrelation and matched filtering in 3D. Various more complicated algorithms based on feature identification and/or machine learning may be implemented to complete 3D registration as well [118].

Other methods of registration along the x-axis and z-axis may be used for imaging more general objects. For example, symmetry of intensity data may be used to center-align and register the objects if they are nearly cylindrically symmetric, including most fiber and samples in capillaries. This technique could also slightly improve program runtime.

5.3 Future Work in Characterizing Additional Types of FBGs

The few samples imaged in this research exemplify exciting new levels of characterization made possible by TDPM, but the analysis of the resulting data remains at least somewhat speculative until further imaging of large quantities of similar FBGs are imaged and procedurally analyzed. The kinds of error, noise, and defects that could be present may be better understood as more FBGs are imaged, allowing for better isolation of observed effects. Sheer quantity of samples is crucial in providing enhanced understanding of the results of TDPM imaging of FBGs.

Additionally, FBGs of a wide variety of types must be imaged and characterized. In addition to the kinds of FBGs imaged in this research, several crucial classes of FBGs have yet to be quantitatively imaged with TDPM. Type I*n* gratings should be imaged to reveal the negative index change from the original core medium and provide advanced insight into how they differ from other types of gratings. Discrete-phase-shifting FBGs should be imaged to confirm that their characteristic functions can still be recovered as previously suggested in this thesis by treating the FBG as several sub-FBGs broken up by

each discrete phase shift such that the characteristic functions of the sub-FBGs may be concatenated to return the overall FBG's characteristic functions.

Tilted FBGs should be imaged, as they provide a simple example of a grating which is very clearly not cylindrically symmetric to further test 3D recovery capabilities of TDPM. Any phase-mask-written FBG will not be cylindrically symmetric due to Talbot patterns resulting from the interference effects of the diffracted beams, but these are at least partially negated in amplitude due to y-axis shifting (lack of proper registration along the fiber axis). For the case of tilted FBGs, lack of proper y-axis registration will still lower the apparent amplitude of RI, but the tilt angle itself will not be affected, providing an additional measure of FBG characterization to recover.

Various sampled FBGs should also be imaged to indicate the effects of writing over existing gratings with different writing techniques for each process. Chirped gratings with higher chirped rates made possible by point-by-point writing should be imaged to better quantify chirp rate recovery capabilities. Additional combinations of the types of FBGs, writing techniques, and periods represented in the imaging already completed in this research should also be imaged to isolate variables for better scientific comparison. If reflection spectra are not known upon obtaining a fiber to be imaged (e.g. the fiber was fabricated in-house or the manufacturer does not provide individual spectra for their fabricated fibers), the spectra should be measured with an optical spectrum analyzer (OSA) before imaging to allow for comparison with imaging results. Even if spectra are known at room temperature, spectra should be measured with the FBG at increased temperature in the experimental configuration prior to imaging to account for any thermally induced changes to the core RI and grating period.

Recovered core RI profiles can be converted to corresponding reflectivity spectra through coupled-mode theory to demonstrate accuracy of the reconstructed RI profiles. This approach, however, is limited in meaning because the recovered profile length from the imaging system's field of view may be as low as 1% of the total FBG length. Therefore, the recovered reflection spectrum from the small imaged portion of the FBG will not correspond the total FBG's spectrum. Similarly, the split-step beam propagation method can be used to simulate the reflection spectrum from the full 3D refractive index distribution, but it is also subject to limitations due to the small size of the imaged portion and is additionally limited due to the decreased recovered RI modulation amplitude with the current system. Demonstrating that the 3D spatial RI distributions recovered in this research produce accurate (though partial and attenuated) spectral responses is still an important step in validating the results.

Modeling spectral responses may also be very effective in confirming the relationship between unwanted spectral effects and local defects that can be captured entirely in the imaged portion. Defect identification is an especially important capability introduced by TDPM. When a fabricated fiber demonstrates unwanted spectral components, it is difficult to identify the cause or source. This makes characterization inefficient for improving manufacturing processes if only spectra are known. In addition to the qualitative imaging of defects made possible through TDPM, quantitative defects as small as a micron can be characterized quantitatively through the way they affect the characteristic functions of the FBG, based on Bao's simulations [94]. Thus, FBGs with intentional and unintentional defects should be imaged to confirm the simulated capabilities and investigate flaws in fabrication processes.

The most crucial FBGs yet to be imaged with TDPM are those in multicore fibers. MCFs introduce the most advanced communication and sensing capabilities, as discussed in Chapter 1. Though it is difficult to write significantly different FBGs in the multiple cores if using a phase mask writing technique, it is possible to write distinct FBGs in each core if a focused point-by-point technique is used [119]. Imaging of such distinct FBGs in a multicore fiber (similar to those simulated by Bao [94]) would best demonstrate full 3D characterization capabilities of TDPM.

Some special sensors made of wrapped [56] or bundled [120] fibers with FBGs can act similarly to a multicore fiber with FBGs. These have the advantages of being easier to write than FBGs in MCFs and having increased curvature sensitivity, but they have the disadvantage of being larger, making imaging the entire sensor within a certain field of view more difficult. With the hardware modifications described in section 5.2.3, however, the imaging of some compound fibers could be made feasible. Such bundles can be made to combine any number of distinct writing techniques and grating types into a fused bundle by researchers. Such combination bundles may be able to benefit from the advantages of different types of gratings simultaneously for certain applications.

For sensing applications, external forces such as longitudinal load, bending, and twisting induce a strain throughout the fiber which changes the stress and refractive index distribution to ultimately change the reflection spectra in a way that can be related to the quantities to be sensed. The resulting RI distribution change can be entirely predicted from the shape change of the fiber using fundamental physics. Shape change is directly related to induced strain (the ratio of change in length per unit length). A general form of Hooke's Law relates strain and stress [121], and the Stress-optic law relates stress and RI

[122]. This means that imaging a fiber under external force is not required to predict the effects thereof. However, residual stress characterization is required to account for nonlinear stress-optic effects in this process.

In Figure 5, the abstraction of the QPI step allows it to be substituted with a technique such as the Brace-Köhler compensator method of retardation measurement to then characterize residual stress in 3D with minimal modification to the imaging system and processing algorithms [123, 124]. Theory and testing related to this complementary measurement has been significantly developed in the Georgia Tech Optics Lab. These complementary measurements offer great potential insight into the physical phenomena related to FBG sensing.

5.4 Concluding Remarks

The principal application of this research is in improving industrial manufacturing of FBGs using findings from FBG QPI characterization. New specifications and tolerances may be defined using refractive index. Novel or combined FBG writing techniques may be developed based on improved understanding of the RI distribution of gratings that result from existing techniques. The structural mechanisms that result in these gratings may be better understood through knowledge of the RI distribution. Production quality and effective use of FBGs may shift from an empirical approach toward quantitative, analytical understanding based on high-quality data obtained in this research and related future work.

APPENDIX A

LARGE-SCALE COPIES OF FIGURES 9(C) AND 9(D)

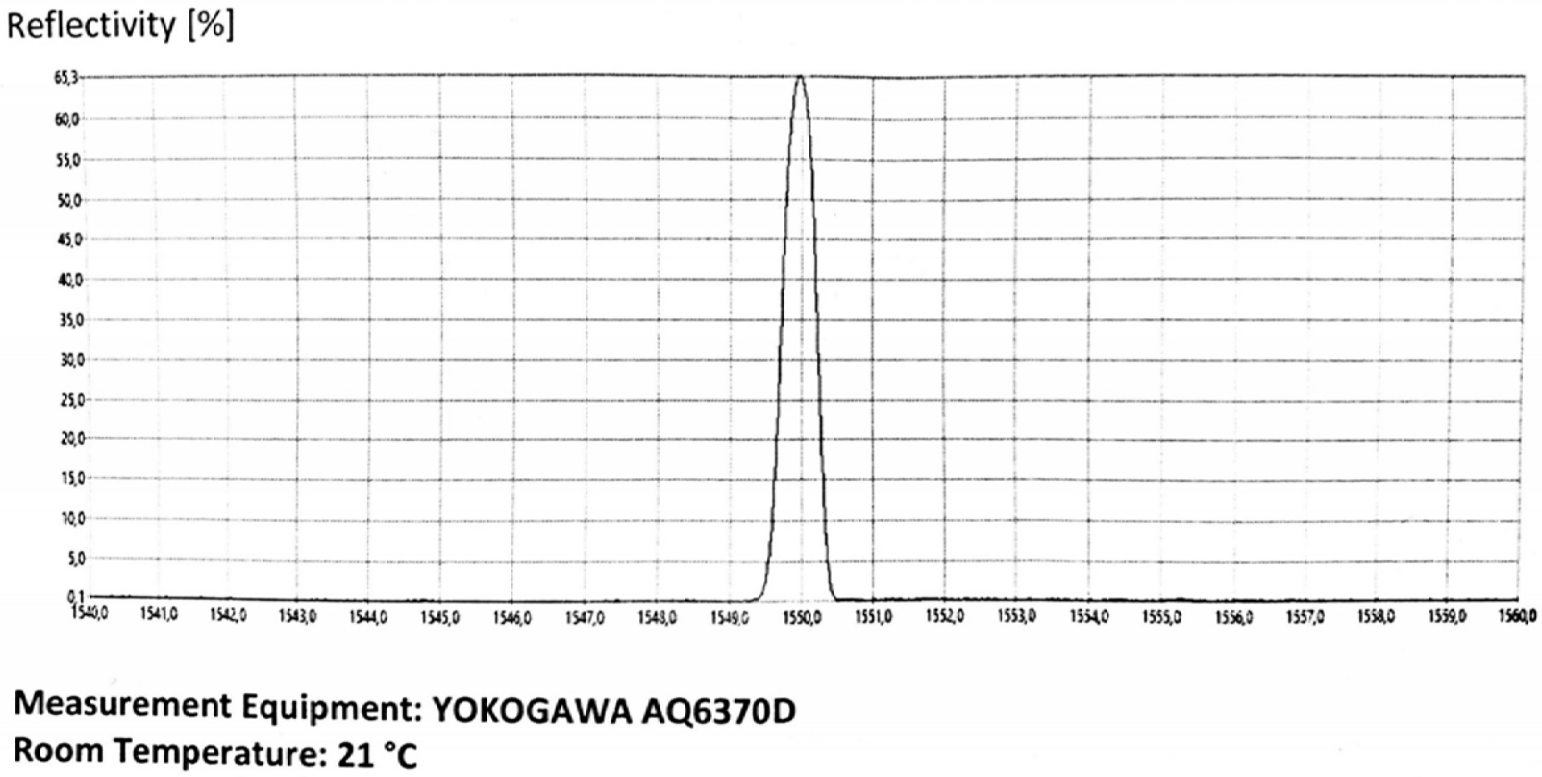

Figure 24. Large-scale copy of Figure 9(c).

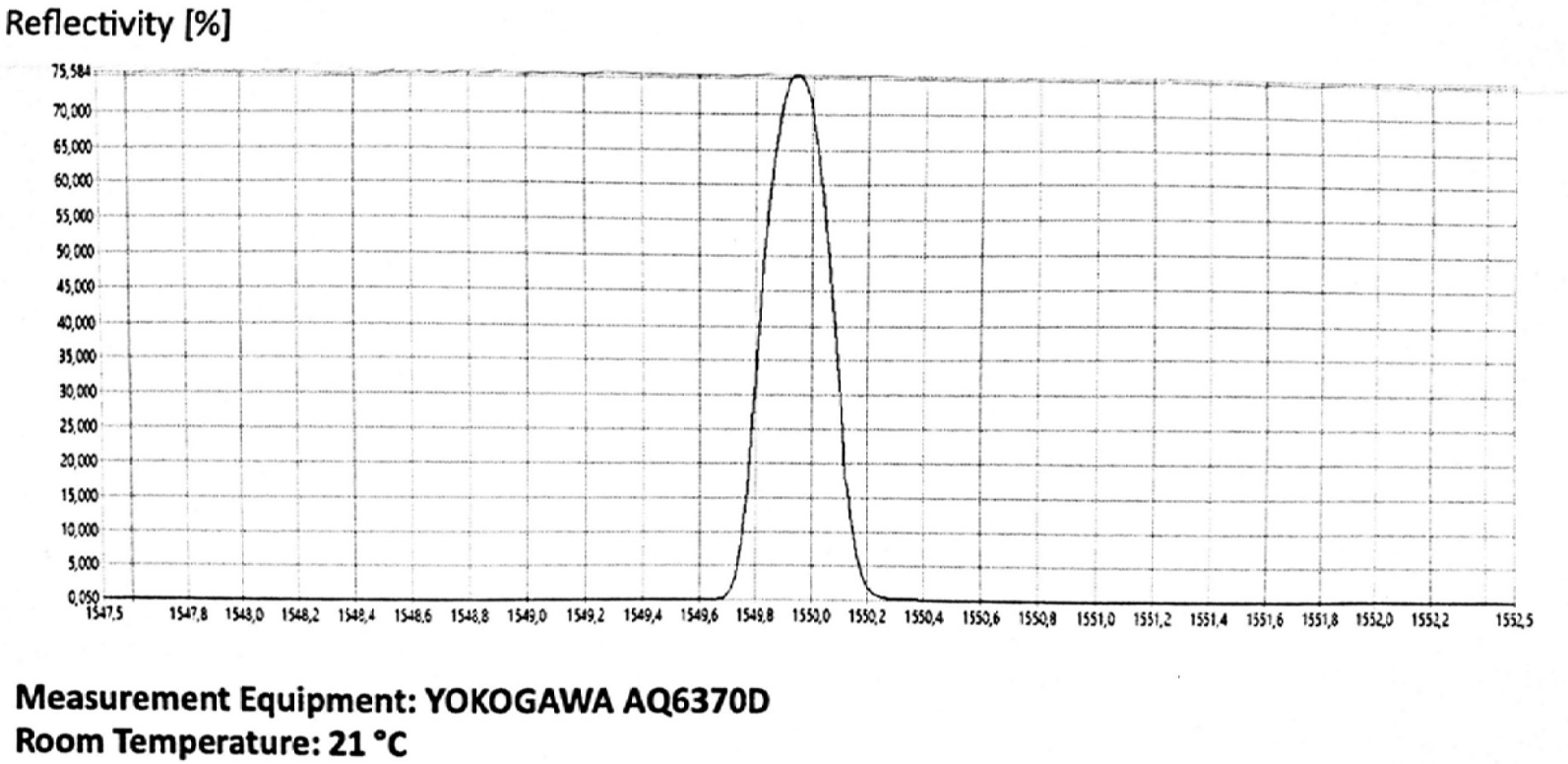

Figure 25. Large-scale copy of Figure 9(d).

APPENDIX B

PERMISSION LETTER FOR REPRINTED MATERIALS

Dear Grayson Noah,

Thank you for contacting The Optical Society.

For the use of figures 1 and 3 from **[1]** Yijun Bao and Thomas K. Gaylord, "Quantitative phase imaging of fiber Bragg gratings in multicore fibers," Appl. Opt. 57, 10062-10071 (2018) and figures 4 and 5 from **[2]** Micah H. Jenkins and Thomas K. Gaylord, "Three-dimensional quantitative phase imaging via tomographic deconvolution phase microscopy," Appl. Opt. 54, 9213-9227 (2015):

> OSA considers your requested use of its copyrighted material to be Fair Use under United States Copyright Law. It is requested that a complete citation of the original material be included in any publication.

While your publisher should be able to provide additional guidance, OSA prefers the below citation formats:

> For citations in figure captions:
>
> [Reprinted/Adapted] with permission from ref [x], [Publisher]. (with full citation in reference list)
>
> For images without captions:
>
> Journal Vol. #, first page (year published) An example: Appl. Opt. 57, 10062 (2018)

Please let me know if you have any questions.

Kind Regards,

Rebecca Robinson

Rebecca Robinson
April 22, 2019
Authorized Agent, The Optical Society

The Optical Society (OSA)
2010 Massachusetts Ave., NW
Washington, DC 20036 USA
www.osa.org

REFERENCES

[1] K. O. Hill, B. Malo, F. Bilodeau, D. C. Johnson, and J. Albert, "Bragg gratings fabricated in monomode photosensitive optical fiber by UV exposure through a phase mask," *Appl. Phys. Lett.,* vol. 62, pp. 1035-7, 1993.

[2] A. Othonos and X. Lee, "Novel and improved methods of writing Bragg gratings with phase masks," *IEEE Photonics Technol. Lett.,* vol. 7, pp. 1183-1185, Oct. 1995.

[3] Y. Qiu, Y. Sheng, and C. Beaulieu, "Optimal phase mask for fiber Bragg grating fabrication," *J. Lightwave Technol.,* vol. 17, pp. 2366-70, Nov. 1999.

[4] B. A. Tahir, J. Ali, and R. A. Rahman, "Fabrication of fiber grating by phase mask and its sensing application," *Journal of Optoelectronics and Advanced Materials,* vol. 8, p. 6, Aug. 2006.

[5] K. O. Hill, B. Malo, K. A. Vineberg, F. Bilodeau, D. C. Johnson, and I. Skinner, "Efficient mode conversion in telecommunication fibre using externally written gratings," *Electron. Lett.,* vol. 26, pp. 1270-2, Aug. 2, 1990.

[6] B. Malo, K. O. Hill, F. Bilodeau, D. C. Johnson, and J. Albert, "Point-by-point fabrication of micro-Bragg gratings in photosensitive fibre using single excimer pulse refractive index modification techniques," *Electron. Lett.,* vol. 29, pp. 1668-1669, Sep. 2, 1993.

[7] V. Mizrahi, S. LaRochelle, G. I. Stegeman, and J. E. Sipe, "Physics of photosensitive-grating formation in optical fibers," *Physical Review A (Atomic, Molecular, and Optical Physics),* vol. 43, pp. 433-8, 1991.

[8] C. M. Rollinson, S. A. Wade, G. W. Baxter, and S. F. Collins, "Imaging of various optical fiber Bragg gratings using differential interference contrast microscopy: Analysis and comparison," *Appl. Opt.,* vol. 55, pp. 783-790, 2016.

[9] N. M. Dragomir, C. Rollinson, S. A. Wade, A. J. Stevenson, S. F. Collins, G. W. Baxter, P. M. Farrell, and A. Roberts, "Nondestructive imaging of a type I optical fiber Bragg grating," *Opt. Lett.,* vol. 28, pp. 789-791, May 15, 2003.

[10] E. Li, X. Wang, and C. Zhang, "Fiber-optic temperature sensor based on interference of selective higher-order modes," *Appl. Phys. Lett.,* vol. 89, Aug. 31, 2006.

[11] G. Lenz, B. J. Eggleton, and N. Litchinitser, "Pulse compression using fiber gratings as highly dispersive nonlinear elements," *J. Opt. Soc. Am. B,* vol. 15, pp. 715-21, Feb. 1998.

[12] T. Komukai, K. Tamura, and M. Nakazawa, "Efficient 0.04-nm apodized fiber Bragg grating and its application to narrow-band spectral filtering," *IEEE Photonics Technol. Lett.,* vol. 9, pp. 934-936, Jul. 1997.

[13] J. Canning, D. C. Psaila, Z. Brodzeli, A. Higley, and M. Janos, "Characterization of apodized fiber Bragg gratings for rejection filter applications," *Appl. Opt.,* vol. 36, pp. 9378-82, Dec. 20, 1997.

[14] R. Kashyap, *Fiber Bragg Gratings*. San Diego: Academic Press, 1999.

[15] T. Erdogan, "Fiber grating spectra," *J. Lightwave Technol.,* vol. 15, pp. 1277-94, Aug. 1997.

[16] K. Ennser, N. Zervas, and R. L. Laming, "Optimization of apodized linearly chirped fiber gratings for optical communications," *IEEE J. Quantum Electron.,* vol. 34, pp. 770-8, May 1998.

[17] D. Pastor, J. Capmany, D. Ortega, V. Tatay, and J. Marti, "Design of apodized linearly chirped fiber gratings for dispersion compensation," *J. Lightwave Technol.,* vol. 14, pp. 2581-2588, Nov. 1996.

[18] C. Chen, Y.-S. Yu, R. Yang, C. Wang, J.-C. Guo, Y. Xue, Q.-D. Chen, and H.-B. Sun, "Reflective optical fiber sensors based on tilted fiber Bragg gratings fabricated with femtosecond laser," *J. Lightwave Technol.,* vol. 31, pp. 455-460, Feb. 1, 2013.

[19] Y. Miao, B. Liu, W. Zhang, B. Dong, H. Zhou, and Q. Zhao, "Dynamic temperature compensating interrogation technique for strain sensors with tilted fiber Bragg gratings," *IEEE Photonics Technol. Lett.,* vol. 20, pp. 1393-1395, Aug. 15, 2008.

[20] K. S. Feder, P. S. Westbrook, J. Ging, P. I. Reyes, and G. E. Carver, "In-fiber spectrometer using tilted fiber gratings," *IEEE Photonics Technol. Lett.,* vol. 15, pp. 933-5, Jul. 2003.

[21] K. S. Lee and T. Erdogan, "Fiber mode conversion with tilted gratings in an optical fiber," *J. Opt. Soc. Am. A,* vol. 18, pp. 1176-1185, May 2001.

[22] P. Petruzzi, C. Lowry, and P. Sivanesan, "Dispersion compensation using only fiber Bragg gratings," *IEEE J. Sel. Top. Quantum Electron.,* vol. 5, pp. 1339-1344, Sep./Oct. 1999.

[23] J. A. J. Fells, S. E. Kanellopoulos, P. J. Bennett, V. Baker, H. F. M. Priddle, W. S. Lee, A. J. Collar, C. B. Rogers, D. P. Goodchild, R. Feced, B. J. Pugh, S. J. Clements, and A. Hadjifotiou, "Twin fiber grating tunable dispersion compensator," *IEEE Photonics Technol. Lett.,* vol. 13, pp. 984-6, Sep. 2001.

[24] B. J. Eggleton, J. A. Rogers, P. S. Westbrook, and T. A. Strasser, "Electrically tunable power efficient dispersion compensating fiber Bragg grating," *IEEE Photonics Technol. Lett.,* vol. 11, pp. 854-6, Jul. 1999.

[25] N. M. Litchinitser and D. B. Patterson, "Analysis of fiber Bragg gratings for dispersion compensation in reflective and transmissive geometries," *J. Lightwave Technol.,* vol. 15, pp. 1323-1328, Aug. 1997.

[26] C. Martinez and P. Ferdinand, "Analysis of phase-shifted fiber Bragg gratings written with phase plates," *Appl. Opt.,* vol. 38, pp. 3223-3228, May 20, 1999.

[27] L. Wei and J. W. Y. Lit, "Phase-shifted Bragg grating filters with symmetrical structures," *J. Lightwave Technol.,* vol. 15, pp. 1405-1409, Aug. 1997.

[28] G. P. Agrawal and S. Radic, "Phase-shifted fiber Bragg gratings and their application for wavelength demultiplexing," *IEEE Photonics Technol. Lett.,* vol. 6, pp. 995-997, Aug. 1994.

[29] P. Petropoulos, M. Ibsen, M. N. Zervas, and D. J. Richardson, "Generation of a 40-GHz pulse stream by pulse multiplication with a sampled fiber Bragg grating," *Opt. Lett.,* vol. 25, pp. 521-523, Apr. 15, 2000.

[30] M. Ibsen, M. K. Durkin, M. J. Cole, and R. I. Laming, "Sinc-sampled fiber Bragg grating for identical multiwavelength operation," in *OFC '98 Optical Fiber Commun. Conf.*, Washington, DC, 1998, pp. 5-6.

[31] L. Hongpu, L. Ming, S. Yunlong, and J. E. Rothenberg, "Advances in the design and fabrication of high-channel-count fiber Bragg gratings," *J. Lightwave Technol.,* vol. 25, pp. 2739-50, 2007.

[32] R. Mahakud, O. Prakash, J. Kumar, S. V. Nakhe, and S. K. Dixit, "Analysis on the effect of UV beam intensity profile on the refractive index modulation in phase mask based fiber Bragg grating writing," *Opt. Commun.,* vol. 285, pp. 5351-5358, Aug. 23, 2012.

[33] D. Mechin, P. Grosso, and D. Bosc, "Add-drop multiplexer with UV-written Bragg gratings and directional coupler in SiO_2-Si integrated waveguides," *J. Lightwave Technol.,* vol. 19, pp. 1282-1286, Sep. 2001.

[34] A. V. Tran, W. D. Zhong, R. S. Tucker, and K. Song, "Reconfigurable multichannel optical add-drop multiplexers incorporating eight-port optical circulators and fiber Bragg gratings," *IEEE Photonics Technol. Lett.,* vol. 13, pp. 1100-1102, Oct. 2001.

[35] S. Abad, M. Lopez-Amo, F. M. Araujo, L. A. Ferreira, and J. L. Santos, "Fiber Bragg grating-based self-referencing technique for wavelength-multiplexed intensity sensors," *Opt. Lett.,* vol. 27, pp. 222-4, Feb. 15, 2002.

[36] H. Kumazaki, Y. Yamada, H. Nakamura, S. Inaba, and K. Hane, "Tunable wavelength filter using a Bragg grating fiber thinned by plasma etching," *IEEE Photonics Technol. Lett.,* vol. 13, pp. 1206-1208, Nov. 2001.

[37] C. Zhang, L. Wang, S. Perumal, K. Qiu, and H. Zhou, "All-optical recognition method of double two-dimensional optical orthogonal codes-based labels using four-wave mixing," *Opt. Express,* vol. 19, pp. 14937-48, 08/01 2011.

[38] A. F. A. Asha'ari, A. A. A. Bakar, and N. F. Naim, "Design of Optical Frequency Domain Reflectometer (OFDR) interferometer based on Fiber Bragg Grating (FBG) for Passive Optical Network (PON) Monitoring," in *7th IEEE International Conference on Photonics, ICP 2018, April 9, 2018 - April 11, 2018*, Langkawi, Kedah, Malaysia, 2018.

[39] J. Hernandez-Cordero, V. A. Kozlov, A. L. G. Carter, and T. F. Morse, "Fiber laser polarization tuning using a Bragg grating in a Hi-Bi fiber," *IEEE Photonics Technol. Lett.,* vol. 10, pp. 941-3, Jul. 1998.

[40] A. Othonos, L. Xavier, and T. Din Ping, "Spectrally broadband Bragg grating mirror for an erbium-doped fiber laser," *Opt. Engr.,* vol. 35, pp. 1088-92, Apr. 1996.

[41] S. Li and C. Kam Tai, "A novel configuration for multiwavelength actively mode-locked fiber lasers using cascaded fiber Bragg gratings," *IEEE Photonics Technol. Lett.,* vol. 11, pp. 179-81, Feb. 1999.

[42] S.-L. Tsao and J. Wu, "Highly accurate temperature sensor using two fiber Bragg gratings," *IEEE J. Sel. Top. Quantum Electron.,* vol. 2, pp. 894-897, Dec. 1996.

[43] E. J. Friebele, "Fiber Bragg grating strain sensors: present and future applications in smart structures," *OPN Optics & Photonics News,* vol. 9, pp. 33-7, Aug. 1998.

[44] V. M. Murukeshan, P. Y. Chan, L. S. Ong, and A. Asundi, "Intracore fiber Bragg gratings for strain measurement in embedded composite structures," *Appl. Opt.,* vol. 40, pp. 145-149, Jan. 1, 2001.

[45] M. Froggatt and J. Moore, "Distributed measurement of static strain in an optical fiber with multiple Bragg gratings at nominally equal wavelengths," *Appl. Opt.,* vol. 37, pp. 1741-6, Apr. 1, 1998.

[46] K. Saitoh and S. Matsuo, "Multicore fibers for large capacity transmission," *Nanophotonics,* vol. 2, pp. 441-454, 2013.

[47] K. Saitoh and S. Matsuo, "Multicore fiber technology," *J. Lightwave Technol.,* vol. 34, pp. 55-66, Jan. 1, 2016.

[48] T. Tenderenda, M. Murawski, M. Szymanski, L. Szostkiewicz, M. Becker, M. Rothhardt, H. Bartelt, P. Mergo, K. Skorupski, P. Marc, L. R. Jaroszewicz, and T. Nasilowski, "Fiber Bragg grating inscription in few-mode highly birefringent microstructured fiber," *Opt. Lett.,* vol. 38, pp. 2224-2226, Jul. 1, 2013.

[49] X. Zhang and W. Peng, "fiber Bragg grating inscribed in dual-core photonic crystal fiber," *IEEE Photonics Technol. Lett.,* vol. 27, pp. 391-394, Feb. 15, 2015.

[50] K. Stępień, M. Slowikowski, T. Tenderenda, M. Murawski, M. Szymanski, L. Szostkiewicz, M. Becker, M. Rothhardt, H. Bartelt, P. Mergo, L. R. Jaroszewicz, and T. Nasilowski, "Fiber Bragg gratings in hole-assisted multicore fiber for space division multiplexing," *Opt. Lett.,* vol. 39, pp. 3571-3574, Jun. 15, 2014.

[51] M. J. Gander, D. Macrae, E. A. C. Galliot, R. McBride, J. D. C. Jones, P. M. Blanchard, J. G. Burnett, A. H. Greenaway, and M. N. Inci, "Two-axis bend measurement using multicore optical fibre," *Opt. Commun.,* vol. 182, pp. 115-121, Aug. 1, 2000.

[52] G. M. H. Flockhart, W. N. MacPherson, J. S. Barton, J. D. C. Jones, L. Zhang, and I. Bennion, "Two-axis bend measurement with Bragg gratings in multicore optical fiber," *Opt. Lett.,* vol. 28, pp. 387-389, Mar. 15, 2003.

[53] D. Barrera, I. Gasulla, and S. Sales, "Multipoint two-dimensional curvature optical fiber sensor based on a nontwisted homogeneous four-core fiber," *J. Lightwave Technol.,* vol. 33, pp. 2445-2450, Jun. 15, 2015.

[54] C. Ledermann, H. Pauer, and H. Woern, "Fiber optical sensor system for shape and haptics for flexible instruments in minimally invasive surgery: overview and status quo," *Proc. SPIE,* vol. 9157, pp. 915766-1--915766-4, 2014.

[55] A. Gillooly, "Medical fiber-optic sensors offer haptics, 3D shape sensing, and pressure sensing," *Laser Focus World,* vol. 52, pp. 43-46, Aug. 2016.

[56] X. Ran, A. Yurkewich, and R. V. Patel, "Curvature, Torsion, and Force Sensing in Continuum Robots Using Helically Wrapped FBG Sensors," *IEEE Robotics and Automation Letters,* vol. 1, pp. 1052-9, 07/ 2016.

[57] D. Leduc, X. Chapeleau, C. Lupi, F. Lopez Gejo, M. Douay, R. Le Ny, and C. Boisrobert, "Experimental synthesis of fibre Bragg gratings index profiles: comparison of two inverse scattering algorithms," *Meas. Sci. Technol.,* vol. 18, p. 12, Nov. 23, 2007.

[58] A. Rosenthal and M. Horowitz, "Inverse scattering algorithm for reconstructing strongly reflecting fiber Bragg gratings," *IEEE J. Quantum Electron.,* vol. 39, pp. 1018-1026, Aug. 2003.

[59] S. Keren, A. Rosenthal, and M. Horowitz, "Measuring the structure of highly reflecting fiber Bragg gratings," *IEEE Photonics Technol. Lett.,* vol. 15, pp. 575-577, Apr. 2003.

[60] G. A. Cranch and G. M. H. Flockhart, "Tools for synthesising and characterising Bragg grating structures in optical fibres and waveguides," *J. Mod. Opt.,* vol. 59, pp. 493-526, Mar. 20, 2012.

[61] R. J. Espejo, M. Svalgaard, and S. D. Dyer, "Characterizing fiber Bragg grating index profiles to improve the writing process," *IEEE Photonics Technol. Lett.,* vol. 18, pp. 2242-2244, 2006.

[62] X. Chapeleau, D. Leduc, C. Lupi, F. López-Gejo, M. Douay, R. Le Ny, and C. Boisrobert, "Local characterization of fiber-Bragg gratings through combined use of low-coherence interferometry and a layer-peeling algorithm," *Appl. Opt.,* vol. 45, pp. 728-735, Feb. 1, 2006.

[63] D.-W. Huang and C.-C. Yang, "Reconstruction of fiber grating refractive-index profiles from complex Bragg reflection spectra," *Appl. Opt.,* vol. 38, pp. 4494-4499, Jul. 20, 1999.

[64] Z. Zhang, C. Tian, M. A. F. Roelens, M. R. Mokhtar, P. Petropoulos, D. J. Richardson, and M. Ibsen, "Direct characterization of the spatial effective refractive index profile in Bragg gratings," *IEEE Photonics Technol. Lett.,* vol. 17, pp. 2685-2687, Dec. 2005.

[65] C. C. Cheng, Y. L. Lo, W. Y. Li, C. T. Kuo, and H. C. Cheng, "Estimations of fiber Bragg grating parameters and strain gauge factor using optical spectrum and strain distribution information," *Appl. Opt.,* vol. 46, pp. 4555-4562, Jul. 20, 2007.

[66] H.-C. Cheng and Y.-L. Lo, "The synthesis of multiple parameters of arbitrary FBGs via a genetic algorithm and two thermally modulated intensity spectra," *J. Lightwave Technol.,* vol. 23, p. 2158, Jun. 1, 2005.

[67] L. M. Baskin, M. Sumetsky, P. S. Westbrook, P. I. Reyes, and B. J. Eggleton, "Accurate characterization of fiber Bragg grating index modulation by side-diffraction technique," *IEEE Photonics Technol. Lett.,* vol. 15, pp. 449-51, Mar. 2003.

[68] P. A. Krug, R. Stolte, and R. Ulrich, "Measurement of index modulation along an optical fiber Bragg grating," *Opt. Lett.,* vol. 20, pp. 1767-9, Sep. 1, 1995.

[69] H. Kuei-Chu, S. Lih-Gen, H. Wei-Wei, and L. Yinchieh, "Methods of achieving linear index-change response for narrow-band fiber Bragg grating sequential writing," *Opt. Commun.,* vol. 277, pp. 310-14, Sep. 15, 2007.

[70] F. El-Diasty, A. Heaney, and T. Erdogan, "Analysis of fiber Bragg gratings by a side-diffraction interference technique," *Appl. Opt.,* vol. 40, pp. 890-896, Feb. 20, 2001.

[71] N. M. Dragomir, D. Garchev, G. W. Baxter, P. M. Farrell, and A. Roberts, "Nondestructive imaging and characterization of optical fiber Bragg gratings," in *Photonics, Devices, and Systems II*, Prague, Czech Republic, 2003, pp. 182-186.

[72] S. S. Kou, L. Waller, G. Barbastathis, and C. J. R. Sheppard, "Transport-of-intensity approach to differential interference contrast (TI-DIC) microscopy for quantitative phase imaging," *Opt. Lett.,* vol. 35, pp. 447-449, Feb. 1, 2010.

[73] C. Y. Wei, C. C. Ye, S. W. James, P. E. Irving, and R. P. Tatam, "AFM observation of surface topography of fibre Bragg gratings fabricated in germanium–boron codoped fibres and hydrogen-loaded fibres," *Opt. Mater.,* vol. 20, pp. 283-294, Nov./Dec. 2002.

[74] S. T. Huntington, P. Mulvaney, A. Roberts, K. A. Nugent, and M. Bazylenko, "Atomic force microscopy for the determination of refractive index profiles of optical fibers and waveguides: A quantitative study," *J. Appl. Phys.,* vol. 82, pp. 2730-2734, Sep. 15, 1997.

[75] J. D. Mills, C. W. J. Hillman, W. S. Brocklesby, and B. H. Blott, "Evanescent field imaging of an optical fiber Bragg grating," *Appl. Phys. Lett.,* vol. 75, pp. 4058-4060, Dec. 27, 1999.

[76] D. P. Tsai, Y. L. Chung, and A. Othonos, "Subwavelength imaging of an etched fiber with an intracore Bragg grating by apertured photon scanning tunneling microscope," *Proc. SPIE,* vol. 2384, pp. 191-197, 1995.

[77] M. H. Jenkins and T. K. Gaylord, "Three-dimensional quantitative phase imaging via tomographic deconvolution phase microscopy," *Appl. Opt.,* vol. 54, pp. 9213-9227, Nov. 1, 2015.

[78] J. Lim, K. Lee, K. H. Jin, S. Shin, S. Lee, Y. Park, and J. C. Ye, "Comparative study of iterative reconstruction algorithms for missing cone problems in optical diffraction tomography," *Opt. Express,* vol. 23, pp. 16933-16948, Jun. 29, 2015.

[79] A. C. Kak and M. Slaney, *Principles of Computerized Tomographic Imaging*. Philadelphia, PA. Society for Industrial and Applied Mathematics, 1988.

[80] J. A. Rodrigo and T. Alieva, "Rapid quantitative phase imaging for partially coherent light microscopy," *Opt. Express,* vol. 22, pp. 13472-13483, Jun. 2, 2014.

[81] T. Kim, R. Zhou, M. Mir, S. D. Babacan, P. S. Carney, L. L. Goddard, and G. Popescu, "White-light diffraction tomography of unlabelled live cells," *Nat. Photon.,* vol. 8, pp. 256-263, Mar. 1, 2014.

[82] N. Streibl, "Three-dimensional imaging by a microscope," *J. Opt. Soc. Am. A,* vol. 2, pp. 121-127, Feb. 1, 1985.

[83] J. P. Guigay, "Fourier-transform analysis of Fresnel diffraction patterns and in-line holograms," *Optik,* vol. 49, pp. 121-125, 1977.

[84] M. R. Teague, "Deterministic phase retrieval: a Green's function solution," *J. Opt. Soc. Am. A,* vol. 73, pp. 1434-1441, Nov. 1, 1983.

[85] S. S. Kou, L. Waller, G. Barbastathis, P. Marquet, C. Depeursinge, and C. J. R. Sheppard, "Quantitative phase restoration by direct inversion using the optical transfer function," *Opt. Lett.,* vol. 36, pp. 2671-2673, Jul. 15, 2011.

[86] M. H. Jenkins and T. K. Gaylord, "Quantitative phase microscopy via optimized inversion of the phase optical transfer function," *Appl. Opt.,* vol. 54, pp. 8566-8579, Oct. 1, 2015.

[87] A. J. Devaney, "A filtered back-projection algorithm for diffraction tomography," *Ultrasonic Imaging,* vol. 4, pp. 336-350, 1982.

[88] C. Fournier, F. Jolivet, L. Denis, N. Verrier, E. Thiebaut, C. Allier, and T. Fournel, "Pixel super-resolution in digital holography by regularized reconstruction," *Appl. Opt.,* vol. 56, pp. 69-77, Jan. 1, 2017.

[89] R. S. Ruskin, Z. Yu, and N. Grigorieff, "Quantitative characterization of electron detectors for transmission electron microscopy," *J. Struct. Biol.,* vol. 184, pp. 385-393, Dec. 1, 2013.

[90] J. W. Goodman, *Introduction to Fourier Optics*. New York: McGraw-Hill, 1996.

[91] R. G. Lyons, *Understanding Digital Signal Processing* 2nd ed. Prentice Hall PTR, 2004.

[92] R. G. Vaughan, N. L. Scott, and D. R. White, "The theory of bandpass sampling," *IEEE Trans. Signal Process.,* vol. 39, pp. 1973-1984, Sep. 1991.

[93] C. T. Chen, *Signals and Systems*. Oxford University Press, 2004.

[94] Y. Bao and T. K. Gaylord, "Quantitative phase imaging of fiber Bragg gratings in multicore fibers," *Appl. Opt.,* vol. 57, pp. 10062-10071, 2018.

[95] L. Hanzo, *Quadrature amplitude modulation from basics to adaptive trellis-coded, turbo-equalised and space-time coded OFDM, CDMA and MC-CDMA systems*, 2nd ed. Hoboken, NJ: Chichester, 2004.

[96] G. Min, J. W. Kim, W. J. Choi, E. S. Choi, and B. H. Lee, "Tomographic imaging system using digital holographic technique based on integrating four buckets phase shifting interferometry," *Proc. SPIE,* vol. 7568, pp. 756824-1--756824-6, 2010.

[97] Corning, "Corning SMF-28e+ Optical Fiber," Model SMF-28e+, 2014.

[98] T. Feng, M. H. Jenkins, F. Yan, and T. K. Gaylord, "Joint residual stress/refractive index characterization of large-mode-area erbium-doped fibers," *J. Lightwave Technol.,* vol. 31, pp. 2426-2433, Jul. 15, 2013.

[99] QImaging, "Retiga 1300R," Model RET-1300R-F-M-12-C, 2004.

[100] J. A. Rodrigo, J. M. Soto, and T. Alieva, "Fast label-free microscopy technique for 3D dynamic quantitative imaging of living cells," *Biomed. Opt. Express,* vol. 8, pp. 5507-5517, Dec. 1, 2017.

[101] J. Luo, K. Ying, P. He, and J. Bai, "Properties of Savitzky–Golay digital differentiators," *Dig. Sig. Proc.,* vol. 15, pp. 122-136, Mar. 1, 2005.

[102] J. D. Barranco Cruz and E. A. Marti Panameno, "Gaussian beam propagation in a nonlinear medium, solving by split step fourier method," in *Frontiers in Optics, FIO 2012, October 14, 2012 - October 18, 2012*, Rochester, NY, United states, 2012.

[103] Y. Bao and T. K. Gaylord, "Quantitative phase imaging method based on an analytical nonparaxial partially coherent phase optical transfer function," *J. Opt. Soc. Am. A,* vol. 33, pp. 2125-2136, Nov. 1, 2016.

[104] Technica Optical Components, LLC, Atlanta, GA, USA.

[105] FemtoFiberTec GmbH, Berlin, Germany.

[106] Corning, "Corning SMF-28 Ultra Optical Fiber," Model SMF-28 Ultra, 2014.

[107] J. Gowar, *Optical Communication Systems*, 2nd ed. Hempstead, UK: Prentice-Hall, 1993.

[108] H. Zhang, D. Fan, Y. Ma, Z. Xiong, Y. Pang, X. Chen, and C. Zhou, "Interrogation of 5000 ultraweak fiber Bragg grating sensors using optical frequency domain reflectometry," *Opt. Engr.,* vol. 57, 2018.

[109] T. Osuch and Z. Jaroszewicz, "Analysis of the Talbot effect in apodized diffractive optical elements," *Photonics Letters of Poland,* vol. 1, pp. 190-192, 2009.

[110] M.-S. Kim, T. Scharf, C. Menzel, C. Rockstuhl, and H. P. Herzig, "Phase anomalies in Talbot light carpets of selfimages," *Opt. Express,* vol. 21, pp. 1287-1300, 2013.

[111] G. Srikanth and A. K. Nath, *Laser wavelength considerations for inscription of Fiber Bragg Gratings: specific to applications in fiber lasers and amplifiers* vol. 10, 2008.

[112] M. Altissimo, "E-beam lithography for micro-/nanofabrication," *Biomicrofluidics,* vol. 4, p. 026503, 2010/06/01 2010.

[113] Armed Forces Supply Support Center, "MIL-STD-150A," Washington DC, USA, 1959.

[114] Y. Bao, G. C. Dong, and T. K. Gaylord, "Weighted-least-squares multi-filter phase imaging with partially coherent light: Characteristics of annular illumination," *Appl. Opt.,* vol. 58, pp. 137-146, 2019.

[115] Physik Instrumente, "PIFOC Objective Scanner with Long Travel Range," Model P-725, 2018.

[116] Y. Bao and T. K. Gaylord, "Iterative optimization in tomographic deconvolution phase microscopy," *J. Opt. Soc. Am. A,* vol. 35, pp. 652-660, Apr. 1, 2018.

[117] J. M. Soto, J. A. Rodrigo, and T. Alieva, "Label-free quantitative 3D tomographic imaging for partially coherent light microscopy," *Opt. Express,* vol. 25, pp. 15699-15712, Jul. 10, 2017.

[118] N. Andrade, F. Augusto Faria, and F. Cappabianco, *A Practical Review on Medical Image Registration: From Rigid to Deep Learning Based Approaches*, 2018.

[119] A. Wolf, S. S. Yakushin, M. Y. Kotyushev, A. V. Dostovalov, S. G. Zhuravlev, O. N. Egorova, S. L. Semyonov, and S. Babin, *Femtosecond Pulse Inscription of FBGs in Multicore Fibers and Their Applications*, 2018.

[120] J. Xu, D. Yang, C. Qin, Y. Jiang, L. Sheng, X. Jia, Y. Bai, X. Shen, H. Wang, X. Deng, L. Xu, and S. Jiang, "Study and test of a new bundle-structure riser stress monitoring sensor based on FBG," *Sensors,* vol. 15, pp. 29648-29660, 2015.

[121] D. Gross, W. Hauger, J. Schröder, W. A. Wall, and J. Bonet, *Engineering Mechanics 2: Mechanics of Materials*. Berlin, Germany: Springer Berlin Heidelberg, 2018.

[122] H. Aben and C. Guillemet, *Photoelasticity of Glass*. Berlin, Germany: Springer Berlin Heidelberg, 2012.

[123] M. R. Hutsel, R. Ingle, and T. K. Gaylord, "Accurate cross-sectional stress profiling of optical fibers," *Appl. Opt.,* vol. 48, pp. 4985-4995, Sep. 10, 2009.

[124] M. R. Hutsel, R. R. Ingle, and T. K. Gaylord, "Technique and apparatus for accurate cross-sectional stress profiling of optical fibers," *IEEE T. Instrum. Meas.,* vol. 60, pp. 971-979, Mar. 2011.